# Diamonds I – SIIG MT acquisition and analysis report

Prepared by: Jessica Spratt

Date: March 15th, 2011

## Introduction

As part the Southampton Island Integrated Geoscience (SIIG) Project, designed to better understand the islands mineral and energy resource potential, magnetotelluric (MT) data were collected across Southampton Island, Nunavut. Broadband (BBMT) and long period (LMT) sites were collected during the 2007 and 2008 summer field seasons across the Paleozoic sediments of the Hudson Bay Basin and onto exposed Archean terrane to the northeast (Figure 1). These data are being analyzed under the GEM (Geo Mapping for Energy and Minerals) program that is designed to study the deep lithosphere beneath the Slave and Churchill provinces of northern Canada to understand the potential for diamonds and reduce their exploration risks. Although the Southampton Island MT data were not acquired under the GEM program, they can be used to aid in obtaining its objectives and add to the expanding MT database in Canada's north.

These MT data will enhance and compliment interpretations of previous data collected along the Melville Peninsula, Baffin Island, and a northwest to southeast profile west of Repulse Bay, as well as those proposed to be acquired in the 2011 and 2012 field seasons (Figure 1). All of these surveys will constitute a substantial dataset that will be used to generate a regional 3-dimensional conductivity model in addition to localized 2-D models. The SIIGMT data have been processed using modern, robust, remote-referencing methods and have been analyzed for dimensionality, effects of distortion, and geo-electric strike angles.

## Data Acquisition and processing

Broadband (BBMT) data were collected at a total of 29 site locations using Phoenix Geophysics recording instruments and sensors. BBMT sites were located in 3 main areas: along a 120 km-long profile (profile A) that extends from the Paleozoic sedimentary cover in the southwest to the exposed Archean terrain to the northeast, along a 50 km-long southwest to northeast profile (profile B) that lies wholly within the Paleozoic sediments, as well as at a 3 locations running perpendicular to the north end of the main profile (Figure 2). The electric fields were measured in the 2 horizontal perpendicular directions using lead-lead chloride porous pots, and the magnetic fields were recorded in the 2 horizontal and, where possible, the vertical directions. In the 2007 summer field season BBMT data

were collected at 12 sites, where the magnetic field components were recorded using three separate MTC50 Phoenix coils that were mounted on tripods for orientation and stabilization. Recording time for these sites ranged from 1 to 20 hours (table 1). In the 2008 summer field, an additional 17 BBMT sites were acquired with the horizontal perpendicular coils dug into the earth, and the vertical fields recorded at some locations with an air loop secured in place with rocks. Here the recording times ranged between 32 and 69 hours. The BBMT data were processed from time series to response functions (apparent resistivity and phase curves) using robust remote reference techniques (Method 6 in Jones et al., 1989), as implemented by the Phoenix Geophysics software package MT2000, and yielded apparent resistivity and phase response curves in the period range of 0.004 s up to 1,000 s for most sites along the profile (Figure 3a). The data quality is highly variable with some sites showing large error bars and large scatter in the response curves. Two sites with recording times < 4 hours (sites sig011 and sig012) produced extremely poor data quality and have not been used in further analysis. It is believe that wind noise on the tripod and shorter recording times in 2007, in general, resulted in lower quality data than those obtained in the 2008 field season (see Appendix A).

In the 2008 summer field season, long period (LMT) data were collected at 6 sites, most located on exposed Archean intrusive and metamorphic rocks, using the LiMS (Long Period Intelligent Magnetotelluric System) recording instrumentation (Figure 2). The electrical fields were recording in the two horizontal, perpendicular directions using lead-lead-chloride porous pots and the magnetic fields were recorded in the two horizontal, and the vertical direction using a 3-component fluxgate magnetometer. Recording times and locations for each site are shown in table 1. Data were acquired for 4 – 14 days with little interruptions in the data acquisition. These long period MT data were processed using the multi-remote-reference, robust, cascade decimation code of Jones (Jones and Jödicke, 1984), generating apparent resistivity and phase response curves as a function of period for each site. In general the data quality is reasonable with smooth response curves and low error bars from 10 s up to 10,000 s (Figure 3b). At one location both long period and broadband data were collected, site sig202, and the response curves were merged together to generate one file with a period range of 0.004 – 10,000 s, spanning nearly 8 decades (Figure 3c).

Several of the data show out of quadrant phase responses, where the phase of one or both modes goes above 90° or drops below 0° (Figure 3d). This is an indication of current channeling, near surface anisotropy, or 3-dimensional distortion. Out of quadrant phase responses are often observed where there is a high contrast in near surface conductivity values, such as recording data in a sediment filled valley between large resistive mountains, or sites located directly on conductive dykes or faults. It is not possible for these data, at the periods ranges that the phases are out of quadrant, to be accurately

represented with 2-dimensional structure and will be omitted when generating 2-D models of the subsurface. Most of these sites lie at the southwestern end of the survey area, at sites located on the Paleozoic sediments. The detailed geological map shows a series of northeast to southwest trending features interpreted as faults that may be responsible for this distortion (Figure 4).

## Data analysis

### Decomposition Analysis

Each site were analyzed using the Groom-Bailey decomposition techniques to understand the degree of dimensionality, determine the most appropriate geoelectric strike direction where the data are 2-dimensional, and ascertain and remove the effects of galvanic distortion in the data (Groom and Bailey, 1989). Single site decompositions were applied to each of the sites using the method described in McNeice and Jones (2001). Where the phase difference between the TE- and TM-modes is minimal (<10°) the data can be considered 1-dimensional, or independent of the geo-electrical strike angle. Where the phase difference is larger, the data are more dependent on the strike angle, and 2-D models need to be generated at the appropriate geo-electric strike angle in order to accurately represent the subsurface conductivity structure. At short periods, where the fields are penetrating the top few kilometers, the geo-electric strike usually follows geologic trends and these trends can be used to resolve the 90° strike ambiguity inherent in the analysis. Ideally along a profile a model can be generated at one strike angle for all periods; however, where the subsurface structure is complex and this angle changes along profile or with depth, the profile may need to be divided into sections and modelled separately at the appropriate geo-electric strike angles. In some cases, no strike angle can be found that fits the data with a reasonable RMS misfit (< 2) even when no constraints are place on the period bandwidth. This is observed at some sites and, along with large RMS values, the data show highly variable twist or shear values that are descriptors of galvanic distortion (Figure 5). The decomposition analysis suggests that the data may not be accurately represented with a 2-D model and some data at these sites may need to be omitted.

The strike directions resulting from single site, single decade period band decompositions with a 90° ambiguity and an error floor set to 3.5%, equivalent to 2° phase, are shown in figure 6. In general, below 0.01 s most of the sites show low phase differences, suggesting that the data are approximately 1-D. The few exceptions, where the phase difference is higher, show a large scatter in the geo-electric strike angle indicating that localized structures are influencing the data. At periods

between 0.01 and 10 s there is a fairly consistent preferred strike angle of ~33° (-57°) for most of the BBMT sites, regardless of the phase difference. At periods between 10 and 100 s, the BBMT data continue to show a preference of 33°, with the exception of a few sites at the center of profile A. This area corresponds to the location of the sites that have phases out of quadrant or high RMS values and is likely a result of local distortion. The LMT sites, where the phase differences are greatest show a strike preference of roughly 45°. At the longest periods, 100 - 1000 s, there is more scatter in the strike angle with geo-electric strikes as low as 16° (-74°) and higher phase differences, likely an indication of poor data quality at these periods.

Due to the extensive Paleozoic sediment cover, the surficial geology is not sufficient to discern the 90° ambiguity in the geo-electric strike analysis. Limited aeromagnetic data is available for the northeastern part of Southampton Island (Figure 7). This data shows some linear structures that are mostly oblique to the preferred strike angles observed in the decomposition analysis, with the exception of the northernmost LMT sites at periods of 10 - 100 s. The aeromagnetic tilt data suggests that the strike for these corresponds to the transverse electric mode (TE-mode) at 45° (parallel to strike) and the transverse magnetic mode (TM-mode) at -45° (perpendicular to strike). The regional gravity data shows northwest to southeast structure, particularly at the southwest ends of profiles A and B (Figure 8). This indicates that the TE-mode is at a geo-electric strike angle of -57° with the TM-mode at 33°.

The data have been recalculated at strike angles of 33°, 45°, and 16°. Figure 9 shows the misfit values for the whole period range along profile A. Where the misfit value is < 2, a 2-D model can be generated to adequately represent the data. The geo-electric strike angle that best fits most of the sites over most of the period ranges is 33°, however several of the sites at particular frequencies do not fit the data regardless of the strike angle selected. This is consistent with the results of single site, single frequency decomposition analysis. The misfit values for the whole period range along profile B are shown for strikes of 16°, 33°, and 45° (Figure 10). Similar to profile A, the geo-electric strike angle that best fist most of the sites over most of the period range is 33° with the exception of site sig112 and sig116. Site sig112 showed high RMS values and strong twist and shear variations at periods greater between 1-10 s in the decomposition analysis, indicating that these data will not fit at any strike angle at these periods (Figure 5c). Site sig116 showed a preferred strike angle of ~2° at periods below 0.1 s (Figure 6) inconsistent with surrounding sites and likely due to localized 2-D structure. The misfit values for the remaining sites are shown for the same three strike angles (Figure 11). The RMS values are independent of the strike angle suggesting that the data are predominantly 1-D.

Two-dimensional models will be generated along profile A and profile B with the data recalculated at a strike angle of -57°. Models should be generated with and without the misfitting data

in order to asses how these sites effect the conductivity structure and the misfit value of the models to the data.

**Depth estimates**

Rough estimates of penetration depths were determined using Schmucker's c-function analysis, which calculates the depth of maximum eddy current flow (Schmucker, 1970). These show that the data penetration is much greater (> 200 km) at the sites that are located off of the Paleozoic sedimentary cover (Figure 12). Within the Paleozoic sediments, the Red Head Rapids Formation of the Hudson Bay Basin is known to host organic-rich thin shales (Zhang, 2008) that commonly have resistivity values on the order of 10 ohm-m. These low resistivities can cause attenuation of the electric and magnetic fields, preventing penetration into the deep earth. In general, the sites located on the Paleozoic sediments have sufficient penetration to image the crust and uppermost mantle structure, where the sites located on the exposed Archean terrane should be able to image the base of the lithosphere.

**Ocean effects**

It is know that the presence of sea water, a near-surface 3-dimensional conductive body, can have significant effects on MT data, due to the sharp contrast in resistivity between the land and the ocean (Schmucker, 1970, Menveillie et al., 1982). The coastal effects is typically observed in the long period data and the severity of these effects is dependent on the salinity of the sea water, the conductivity structure of the subsurface, the depth of the ocean, and the proximity of the MT site to the coast (eg. Jones, 1981, Santos et al., 2001, Pous et al., 2003). In order to assess the coastal effects on this data set, a 3-D mesh was created with ocean resistivity values of 0.3 ohm-m extending to depths of 500m, (approximated from the International Bathymetric Chart of the Arctic Ocean : http://www.ngdc.noaa.gov/mgg/bathymetry/arctic/arctic.html), and a uniform land resitivity values of 500 ohm-m (Figure 13). A forward inversion then generated synthetic response curves at the recorded site locations. This method of determining coastal effects is an approximation, as the coast line is not exact, the depth and resistivity of the ocean is approximated, and a uniformly resistive earth was used rather than a layered or structured earth. It is therefore only used to illustrate caution in interpreting 2-dimensional models that include long period data near the coast.

The calculated forward response curves show that there is little effect of the ocean on the sites along profile A, those furthest from the coast, where the apparent resistivity and phases are consistent with a uniform half space of 500 ohm-m to periods of nearly 100 s (Figure 13). The strongest effect is

seen at sig205 and sig204, sites nearest the coast, at a periods early as 1s. This implies that it is possible for the LMT data to have coastal effects at the entire recorded period range. Moderate effects are observed at periods as short as 10 s for sites along profile B. Depth analysis, similar to that described above, for site sig117 shows that 10 s corresponds to a depth of 17 km in the xy-mode and 35 km in the yx-mode, suggesting that these sites should be able to accurately image most of the crust. Depth analysis of site sig202 shows that 100 s in the XY mode corresponds to depths of 94 km suggesting that a conductivity model of crust and upper mantle should be relatively unaffected by the ocean.

## Data Modeling

The distortion-corrected, regional 2-D responses from sites along the main northwest to southeast profile have been imported in the WinGlink MT interpretation software package at a geo-electric strike angle of -57°, and 45°(-45° ). Each site in each has been manually edited to remove data points with large error bars or large scatter, and data with phases above 90° or below 0° were removed. The degree of static shift effects on the data cannot be numerically determined. Typically, static shift effects arise from a charge build up at the base of near surface conductors and the effect is to raise the apparent resistivity values of the entire response curve. Where one apparent resistivity curve was much higher than another, the curve was dropped to match that of the other curve at the shortest period. This helps to reduce the effect of anisotropic shift, but does not account for the static shift cases were both curves are affected.

### 1-D Models

One-dimensional layered earth models were generated for each site using Occam's inversion codes as implemented by the WingLink MT interpretation software package and stitched together to create cross-sections along the SIIGMT profiles A and B (Figures 14a and 15a). Pseudosections of the phase responses for each of the sites along the profiles were generated for both the TE- and TM-modes (Figures 14b and 15b). As previously described in the phase difference plots, where these sections are similar, the 1-D models can be considered to be a valid representation of the Earth; however they do not account for static shift effects. Few similarities are observed between the TE- and TM-modes in the 1-D models or the phase pseudosections along both profile A and profile B. This is a strong indication that the data are structurally complex, requiring 2-D or 3-D modelling to image the subsurface. The 1-D models of the TM- and TE-modes have also been generated for the remaining

BBMT sites and the LMT sites (Figure 16). With the exception of site sig206, the models for the two modes show strong similarities indicating that the data are predominantly 1-D and that the subsurface is laterally uniform.

**2-D Models**

As is common with many regularized inversion codes, this 2-D code searches iteratively for the smoothest model that best fits the data by attempting to trade off the fit to the observed data (data misfit) with the squared Laplacian (smoothing term) of the horizontal and vertical resistivity gradients. The inversion program searches for the smoothest, best-fit model with the least deviation from the starting model, which is usually a half space (Mackie and Madden, 1993). This means that the models found represent the minimum structure required to fit the data with an acceptable misfit.

Many different models need to be generated using various combinations of modes and parameters in order to observe the effects of these changes on the model structure and to derive the most robust final model with an appropriate misfit value. Several models were generated from the data along profile A at a geo-electric strike angle of -57°, using the entire period range of 0.004 – 10,000 s of both the TM- and TE-modes. The error floor were set to 30% for the apparent resistivity to account for static shift effects, and 7% for the phase. For each model the smoothness parameter, tau, was changed after 100 iterations in order to determine the most appropriate tau value for the dataset. Figure 17 illustrates the trade-off between the roughness of the model, defined by the tau parameter, and the fit of the model to the data, RMS. This shows that a tau value of 7 would result in the smoothest model with the best fit to the data.

Once an appropriate tau value was determined, using similar error floors for phase and apparent resistivity, several more models were generated along profile A at a strike angle of -57° while varying data components and parameters. Inversions of the TM-mode data alone typically result in models that identify lateral boundaries, but can be insensitive to other electrical structures that the TE-mode data better resolve. The TE-mode data are more sensitive to the conductance of structures, identifying the depth to conductive zones, and thin sub-vertical low-resistivity units. Inversions were initiated with a homogeneous half space of 500 ohm m, a mesh consisting of 64 rows and 178 columns, and a smoothing parameter (tau) of 7. The parameters that were varied include using combinations of the TM and TE mode data, the smoothing parameters alpha and beta that trade-off vertical against horizontal gradient weighting, and the weighting of the regularization order (Figure 18 a-f). Although there are slight variations in the resistivity value and the structures, the general features are consistent between the different models. The model with an alpha value of 1.0 and beta of 1.5 resulted in the smoothest

model with the lowest RMS value (Figure 18d) and has been used for further analysis.

The RMS values, particularly when using both the TM and TE-mode data, are high. Although out of quadrant phases have been omitted from the dataset in these models, single site data with high RMS values (determined during the decomposition analysis) have not yet been removed. The misfit value for each site for the 2-D model along profile A suggests that certain sites with anomalously high values, particularly those at the southwestern-most extent of the profile, may be strongly influencing the overall model RMS value (Figure 19). These sites, in general, are those that resulted in high RMS values in the decomposition analysis described above. Similar models need to be generated without these data in order to assess changes in the subsurface structure and the associated RMS value. Additionally, focused models of particular areas of interest may help to further resolve structure and improve the RMS misfit. When inverting fewer data the responses to local-scale structures have a higher influence on the average misfit value and so can be better represented in the models.

One method of testing the sensitivity of the data to structure at depth is to alter the final 2-D model, run a forward inversion, and compare the resulting model RMS values. This has been done at the southwestern end of profile A by inserting a resistive block at depths between 23 - 50 km into the model (Figure 20). Consistent with the results of penetration depth estimates, the RMS value remains constant at 3.1 after the forward inversion, indicating that these data are not sensitive to this region of the subsurface.

**Preliminary models**

Although these models represent rough preliminary conductivity images, some features appear to be consistent in the data (Figures 18 and 21). The models beneath the exposed Archean terrane show a resistive crust to depths of ~30 km that is underlain by a less resistive lower crust or upper mantle. This is inconsistent with the results along the Melville peninsula that show high resistivities to depths of 35 – 39 km. The models show a change from laterally continuous layers to a more complex structure observed at crustal depths beneath the Paleozoic cover at the southwestern end of profile A and along the entire length of profile B, revealing a decrease in resistivity at a depth of ~10 km. Focussed inversions of this region may help to further resolve the subsurface features. The deep structure along profile A shows a moderately resistive upper mantle (200-300 ohm-m) and an decrease in resistivity at depths ranging between 150 and 250 km (Figure 22); however, this is approaching the maximum penetration depth estimates and sensitivity testing should be applied to verify features at these depths.

## Conclusions

Careful processing and analysis of MT data collected along the Southampton Island Integrated Geoscience Magnetotelluric (SIIGMT) profiles have provided a good understanding of dimensionality, and distortion of the data and show that the quality of the data is sufficient to model the crustal conductivity structure beneath the survey area, and in some cases the entire lithospheric structure. Decomposition analysis shows that a geo-electric strike angle of -57° is appropriate for most of the data at most of the period range along profile A and profile B, and that a strike of 45° and/or -45° should be considered for the remaining broadband and long period data. Systematic modeling of the data using different variables has helped to determine some of the inversion parameters that should be used to provide an accurate image of the subsurface. Preliminary 1-D and 2-D models reveal some structure that appears to be consistent in the data. These models also illustrate the need for additional 2-D and 3-D inversions to further resolve the subsurface conductivity structure.

### References


Groom, R.W., and R.C. Bailey, 1989: Decomposition of magnetotelluric impedance tensors in the presence of local three-dimensional galvanic distortion; Journal of Geophysical Research, v. 94, p. 1913 – 1935.

Heywood, W.W. and Sanford, B.V., 1976: Geology of Southampton, Coats and Mansel Islands, District of Keewatin, Northwest Territories; Geological Survey of Canada, Memoir 382, 35p.

A.G. Jones, 1981: Geomagnetic Induction Studies in Scandinavia - II. Geomagnetic Depth Sounding, Induction Vectors and Coast-Effect; Journal of Geophysics, v.50, p. 23 – 36.

Jones, A.G., and H. Jodicke, 1984: Magnetotelluric transfer function estimation improvement by a coherence-based rejection technique, paper presented at the 54th Society of Exploration Geophysics Annual General Meeting, Atlanta, George, 2-6 December, Abstract volume, pp. 51-55.

Jones, A.G., A.D. Chave, G.D. Egbert, D. Auld, and K. Barh, 1989: A comparison of techniques for magnetotelluric response function estimation; Journal of Geophysical Research, v. 94, p. 14210 – 14213.

Mackie, R.L., and T.R. Madden, 1993: Three-dimensional magnetotelluric inversion using conjugate gradients; Geophysical Journal Internations, V. 115, p. 215 – 229.

McNeice, G.W., and A.G. Jones, 2001: Multisite, multifrequency tensor decomposition of magnetotelluric data; Geophysics, v. 66, p. 158 – 173.

Menvielle, M.J.C., P. Rossignal, and P. Tarits, 1982: The coast effect in terms of deviated electric currents: A numerical study; Physics of the Earth and Planetary Interiors, v. 28, p. 118 – 128.

J. Pous, W. Heise, P.A. Schegg, G. Munoz, J. Mart, and C. Soriano, 2002. Magnetotelluric study of the Las Canadas caldera (Tenerife, Canary Islands): structural and hydrogeological implicaions; Earth and Planetary Science Letters, v. 204, p. 249 – 263.

F. A. M. Santos, M. Nolasco, E. P. Almeida, J.Pous-and L.A. Mendes-Victor: 2001. Coast effects on magnetic and magnetotelluric transfer functions and their correction: application to MT soundings carried out in SW Iberia; Earth and Planetary Science Letters, v.186, p. 283-295.

Schmucker, U., 1970. Anomalies of geomagnetic variations in the southwestern United States, Bull. Scripps Ints. Oceanogr. v. 13, 165 p.

Zhang, S. 2008. New insights into the Ordovician oil shales in Hudson Bay Basin: their number, stritigraphic position, and petroleum potential; Bulletin of Canadian Petroleum Geology, v. 56, n. 4, p. 300 - 324.

**Figure Captions**

Figure 1: Regional map illustrating the locations of MT surveys in eastern Nunavut: CBEX= the Central Baffin Magnetotelluric Experiment, MPMT = Melville Peninsula Magnetotelluric survey, SIIGMT = Southampton Island Integrated Geoscience Magnetotelluric survey, DMT1 = Diamonds Magnetotelluric survey: corridor 1, CPMT - Cumberland Peninsula Magnetotelluric survey, and STZMT - Snowbird Tectonic Zone Magnetotelluric survey.

Figure 2: Simplified geological map of Southampton Island showing the location of magnetotelluric sites recorded. The circles mark the locations of the response curve examples shown in figure 4. The grey lines show the position of the profiles used for 2D modelling.

Figure 3: Examples of apparent resistivity and phase MT response curves for data measured at 4 sites: (a) shows an examples of the broadband data, (b) shows an example of the long period data, (c) shows the merged broadband and long period data, and (d) shows an example of data distortion causing the

phases of one mode to be out of quadrant.

Figure 4: Detailed geological map of Southampton Island showing mapped structural features in relation to MT site locations. Map modified from Heywood and Sanford, 1976. The black circles mark the sites that have phases out of quadrant at a strike angle of -57°.

Figure 5: Examples of results of single-site, single-frequency decomposition analysis: (a) shows a site with strong twist and shear variations, (b) and (c) show examples of high RMS values corresponding to high twist and shear values suggestive of the presence of local 3-D distortion.

Figure 6: Maps showing the preferred geo-electric strike direction with a 90º ambiguity at each site for single decade period bands. The color scale illustrates the maximum difference between the TM- and TE-mode phases.

Figure 7: Map of the MT survey area showing the available aeromagnetic tilt data. The arrows show the preferred geo-electric strike direction at the 0.01 - 0.1 s and the 10 - 100 s period bandwidths, the length of the arrow is scaled by the maximum phase difference between the TM and TE modes.

Figure 8: Map of the MT survey area showing the regional gravity data. The arrows show the preferred geo-electric strike direction at the 0.01 - 0.1 s and 0.1 - 1 s period bandwidths, and the length of the arrow is scaled by the maximum phase difference between the TM and TE modes.

Figure 9: Data misfit values at sites along profile A over the whole recorded period range for data recalculated at a geo-electric strike direction of 16º (a), 33º (b), and 45º (c). The red ellipses mark areas that do not fit at any strike angle, evidence for distortion. The black ellipses mark sites that showed either high RMS values or highly variable twist and shear values in the single-site, single-frequency decomposition analysis.

Figure 10: Data misfit values at sites along profile B over the whole recorded period range, for data

recalculated at a geo-electric strike direction of 16º (a), 33º (b), and 45º (c). The red ellipses mark the areas that do not fit at any strike angle. The black ellipse marks the site that showed high RMS values in the single-site, single-frequency decomposition analysis.

Figure 11: Data misfit values at the northernmost broadband sites and the long period sites over the whole recorded period range, for data recalculated at a geo-electric strike direction of 16º (a), 33º (b), and 45º (c). The red ellipses mark the areas that do not fit at any strike angle. The black ellipses mark sites that showed highly variable twist and shear values at short periods in single-site, single-frequency decomposition analysis.

Figure 12: Estimates of maximum penetration depths for each site along profile A (a), profile B (b), and the northern broadband and long period sites (c) in both the mutually perpendicular XY and YX modes. The black circles mark sites where phases are out of quadrant, an indication of distortion.

Figure 13: A 3-D mesh of the MT survey area showing the land versus ocean conductivity contrast. Examples of the forward calculated response curves are shown for sites sig204, sig010, sig117, sig103, and sig101.

Figure 14: Cross-section along profile A illustrating the results of 1-dimensional Occam inversions (a) and pseudosections of the phases along profile B with increasing period of both the TE- and TM-modes (b).

Figure 15: Cross-section along profile B illustrating the results of 1-dimensional Occam inversions (a) and pseudosections of the phases along profile B with increasing period of both the TE- and TM-modes (b).

Figure 16: Results of 1-dimensional Occam inversions of the northernmost broadband sites and the long period sites for both the TM- and TE-modes.

Figure 17: Graph illustrating the trade-off between the RMS misfit of the model to the data and the tau value of the inversion. The tau value chosen for subsequent 2-D models is 7.

Figure 18: Preliminary 2-D models of the MT data along profile A, at a strike angle of -57°, using various data components and variables after 100 iterations. The TM-only data and the TM+TE data were used with an alpha value of 1 and a beta value of 1 (a), and (b). The TM-only data and the TM+TE data were used with an alpha value of 1 and a beta value of 1.5 (c) and (d). The TM-only and the TM+TE data were used with an alpha value of 1 and beta value of 0.3 (e) and (f).

Figure 19: RMS values at each site along profile A for the model shown in figure 18d.

Figure 20: Altered 2-D model along profile A generated to test the sensitivity of the data at depths beneath the southwestern-most sites.

Figure 21: Preliminary 2-D models of the MT data along profile B, at a strike angle of -57° using various data components and variables after 100 iterations. The TM-only data and the TM+TE data were used with an alpha value of 1 and a beta value of 1 (a), and (b). The TM-only data and the TM+TE data were used with an alpha value of 1 and a beta value of 1.5 (c) and (d).

Figure 22: Preliminary 2-D model of the MT data along profile A, at a strike angle of -57°, shown to 300 km depth.

| Site Name | Data Range | Latitude | Longitude | Start Date | Start Time | End Date | End Time | Duration of acquisition |
|---|---|---|---|---|---|---|---|---|
| SIG002 | BBMT | -85.007861 | 63.837750 | 17/08/2007 | 14:00 | 17/08/2007 | 21:36 | 7.6 hours |
| SIG003 | BBMT | -84.821694 | 63.999944 | 18/08/2007 | 17:24 | 19/08/2007 | 15:20 | 21.9 hours |
| SIG004 | BBMT | -84.703556 | 64.086806 | 18/08/2007 | 22:56 | 19/08/2007 | 19:08 | 20.2 hours |
| SIG005 | BBMT | -84.563444 | 64.198639 | 19/08/2007 | 17:32 | 20/08/2007 | 13:28 | 19.9 hours |
| SIG006 | BBMT | -84.438389 | 64.294889 | 19/08/2007 | 20:49 | 20/08/2007 | 18:22 | 21.5 hours |
| SIG007 | BBMT | -84.308472 | 64.420139 | 20/08/2007 | 16:13 | 21/08/2007 | 14:00 | 21.8 hours |
| SIG008 | BBMT | -84.461361 | 64.679056 | 20/08/2007 | 20:46 | 21/08/2007 | 14:01 | 17.3 hours |
| SIG009 | BBMT | -84.729556 | 64.756222 | 21/08/2007 | 17:10 | 22/08/2007 | 14:00 | 20.8 hours |
| SIG010 | BBMT | -84.981528 | 64.801389 | 21/08/2007 | 22:45 | 22/08/2007 | 18:00 | 19.2 hours |
| SIG011 | BBMT | -84.935050 | 63.910300 | 25/08/2007 | 15:14 | 25/08/2007 | 18:23 | 3.2 hours |
| SIG012 | BBMT | -85.054767 | 63.786317 | 25/08/2007 | 16:46 | 25/08/2007 | 17:57 | 1.2 hours |
| SIG013 | BBMT | -84.111778 | 64.579722 | 16/08/2007 | 21:29 | 17/08/2007 | 13:02 | 15.6 hours |
| SIG101 | BBMT | -85.106389 | 63.763972 | 12/07/2008 | 23:00 | 14/07/2008 | 15:24 | 40.4 hours |
| SIG102 | BBMT | -85.040722 | 63.795861 | 12/07/2008 | 23:00 | 14/07/2008 | 16:14 | 41.2 hours |
| SIG103 | BBMT | -84.327556 | 64.387528 | 14/07/2008 | 19:00 | 16/07/2008 | 12:18 | 41.3 hours |
| SIG104 | BBMT | -84.211139 | 64.502944 | 14/07/2008 | 20:00 | 17/07/2008 | 11:49 | 63.8 hours |
| SIG105 | BBMT | -84.666667 | 64.119472 | 19/07/2008 | 19:00 | 21/07/2008 | 15:50 | 44.8 hours |
| SIG106 | BBMT | -84.776806 | 64.037611 | 19/07/2008 | 21:00 | 21/07/2008 | 16:20 | 43.3 hours |
| SIG107 | BBMT | -84.844583 | 63.972361 | 21/07/2008 | 18:00 | 23/07/2008 | 02:00 | 32.0 hours |
| SIG108 | BBMT | -84.894667 | 63.921222 | 21/07/2008 | 20:00 | 23/07/2008 | 16:23 | 44.4 hours |
| SIG109 | BBMT | -84.966944 | 63.881861 | 23/07/2008 | 18:00 | 26/07/2008 | 15:11 | 69.2 hours |
| SIG110 | BBMT | -85.191306 | 63.723472 | 23/07/2008 | 20:00 | 25/07/2008 | 17:41 | 45.7 hours |
| SIG111 | BBMT | -85.235556 | 63.683278 | 26/07/2008 | 17:00 | 28/07/2008 | 09:37 | 40.6 hours |
| SIG112 | BBMT | -84.755694 | 63.664361 | 26/07/2008 | 19:00 | 28/07/2008 | 03:23 | 32.4 hours |
| SIG113 | BBMT | -84.599472 | 63.791333 | 29/07/2008 | 20:00 | 01/08/2008 | 03:04 | 55.1 hours |
| SIG114 | BBMT | -84.653389 | 63.748750 | 29/07/2008 | 18:30 | 01/08/2008 | 08:10 | 61.7 hours |
| SIG115 | BBMT | -84.697778 | 63.702722 | 29/07/2008 | 17:30 | 01/08/2008 | 02:01 | 56.5 hours |
| SIG116 | BBMT | -84.538278 | 63.864972 | 01/08/2008 | 22:00 | 04/08/2008 | 06:40 | 56.7hours |
| SIG117 | BBMT | -84.464139 | 63.926500 | 01/08/2008 | 23:00 | 03/08/2008 | 13:02 | 38.0 hours |
| SIG201 | LMT | -84.471667 | 65.280556 | 09/07/2008 | 01:00 | 17/07/2008 | 19:15 | 8.76 days |
| SIG202 | LMT | -84.114167 | 64.576944 | 09/07/2008 | 01:00 | 23/07/2008 | 09:01 | 14.3 days |
| SIG203 | LMT | -84.273333 | 64.924444 | 11/07/2008 | 01:00 | 25/07/2008 | 00:28 | 14.0 days |
| SIG204 | LMT | -81.932500 | 64.275833 | 10/07/2008 | 01:00 | 16/07/2008 | 01:44 | 6.0 days |
| SIG205 | LMT | -83.245556 | 64.151389 | 23/07/2008 | 20:00 | 28/07/2008 | 17:13 | 4.1 days |
| SIG206 | LMT | -83.887222 | 64.105556 | 26/07/2008 | 20:00 | 01/08/2008 | 21:26 | 6.0 days |

Table 1: Site type, location, and recording times for each of the MT sites collected along the Diamonds I profile.

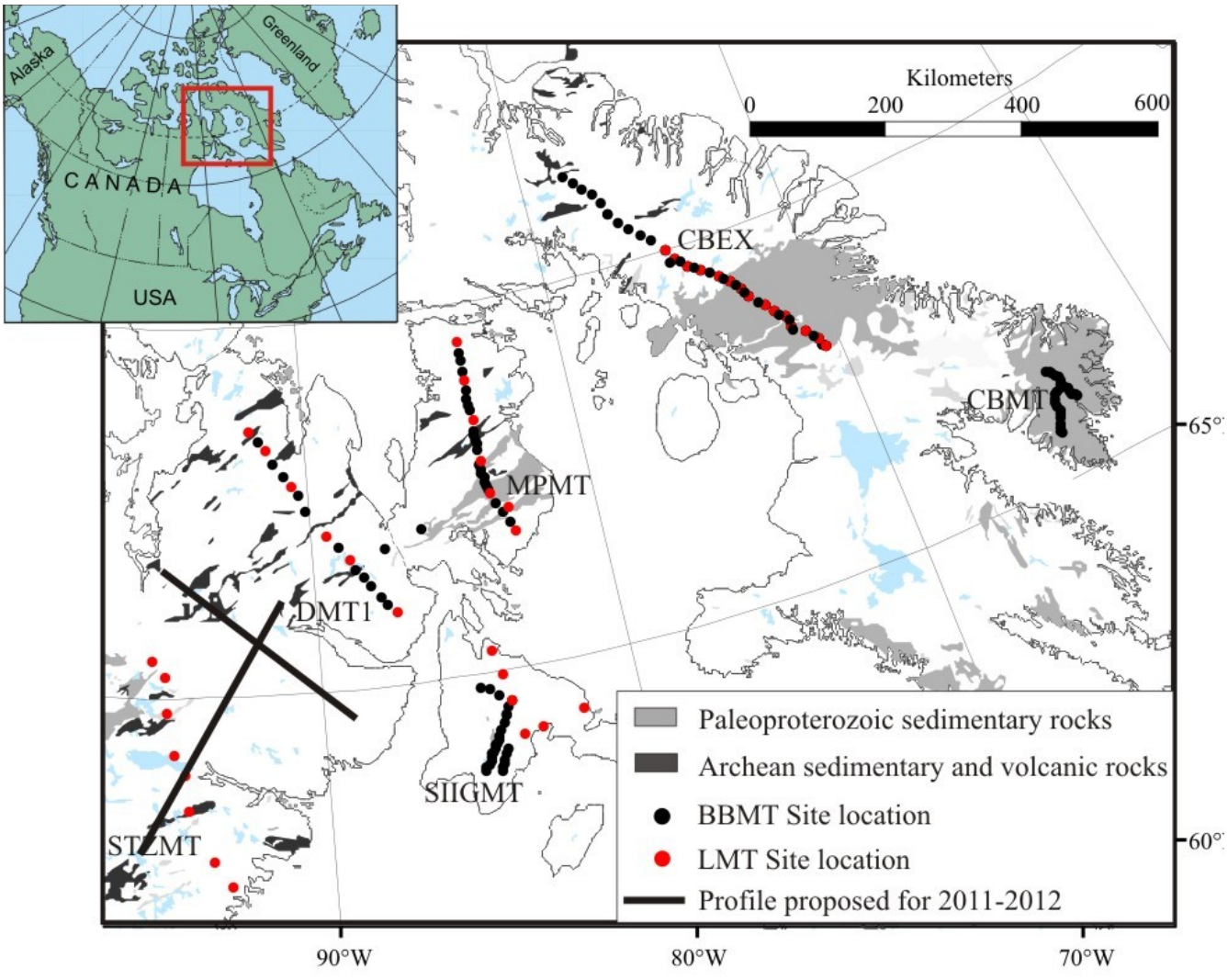
Alaska
Greenland
CANADA
USA
Kilometers
0
200
400
600
CBEX
CBMT
MPMT
DMT1
SIIGMT
STLMT
Paleoproterozoic sedimentary rocks
Archean sedimentary and volcanic rocks
BBMT Site location
LMT Site location
Profile proposed for 2011-2012
65°
60°
90°W
80°W
70°W

Figure 1

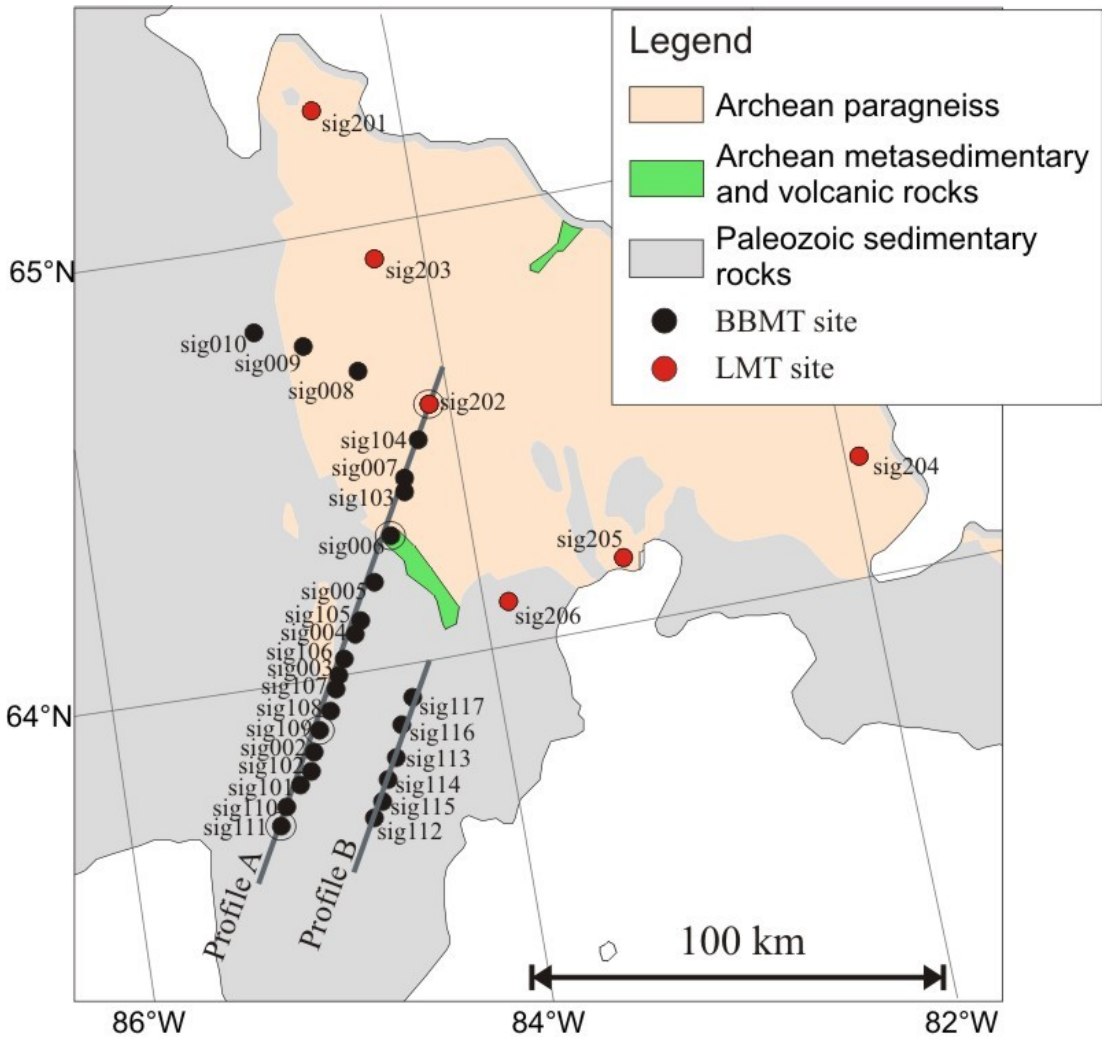
Legend
Archean paragneiss
Archean metasedimentary and volcanic rocks
Paleozoic sedimentary rocks
BBMT site
LMT site
sig201
sig203
sig010
sig009
sig008
sig202
sig104
sig007
sig103
sig006
sig005
sig105
sig004
sig106
sig003
sig107
sig108
sig109
sig002
sig102
sig101
sig110
sig111
sig117
sig116
sig113
sig114
sig115
sig112
sig204
sig205
sig206
Profile A
Profile B
100 km
65°N
64°N
86°W
84°W
82°W

Figure 2

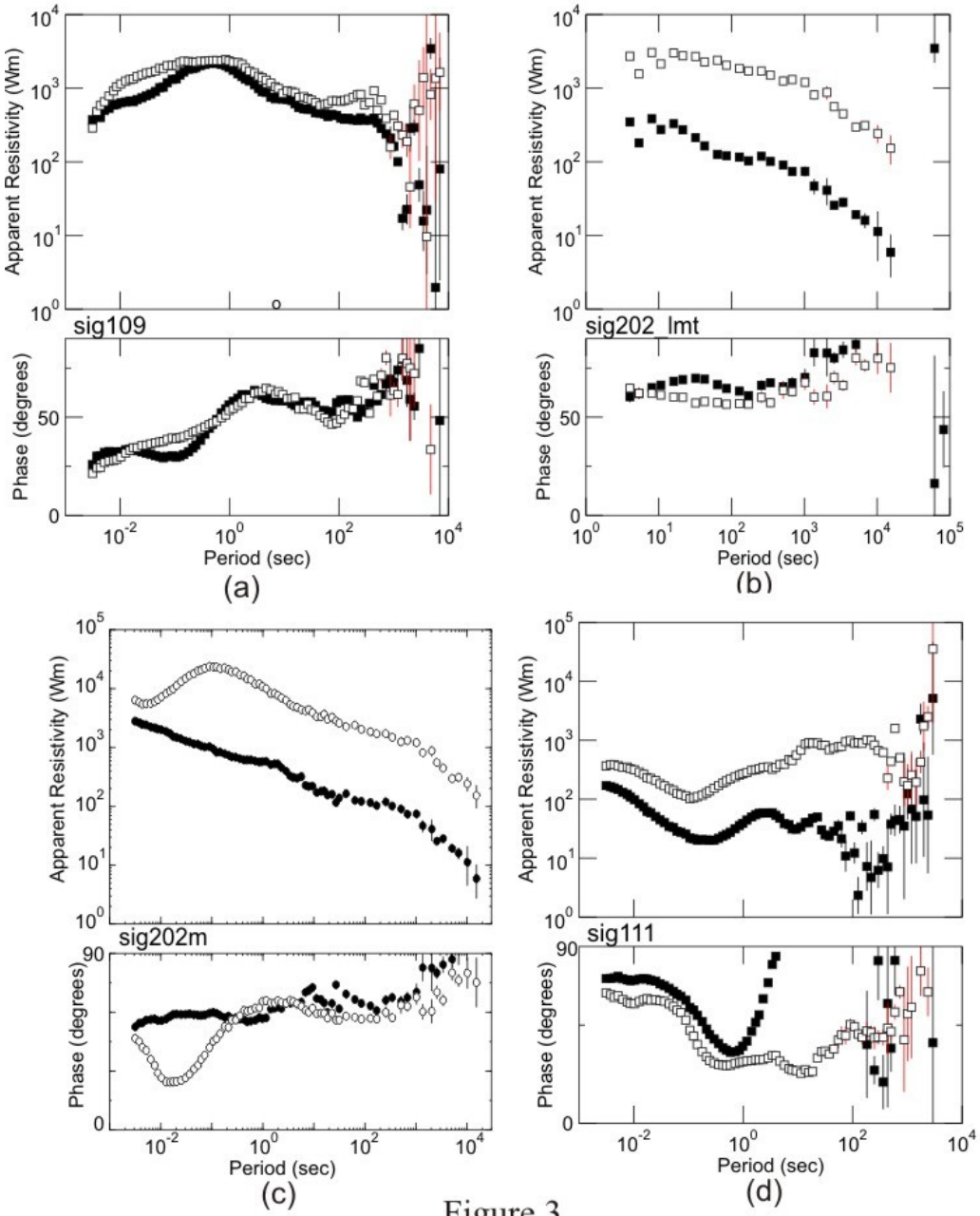
Apparent Resistivity (Wm)
sig109
Phase (degrees)
Period (sec)
(a)
Apparent Resistivity (Wm)
sig202_lmt
Phase (degrees)
Period (sec)
(b)
Apparent Resistivity (Wm)
sig202m
Phase (degrees)
Period (sec)
(c)
Apparent Resistivity (Wm)
sig111
Phase (degrees)
Period (sec)
(d)

Figure 3

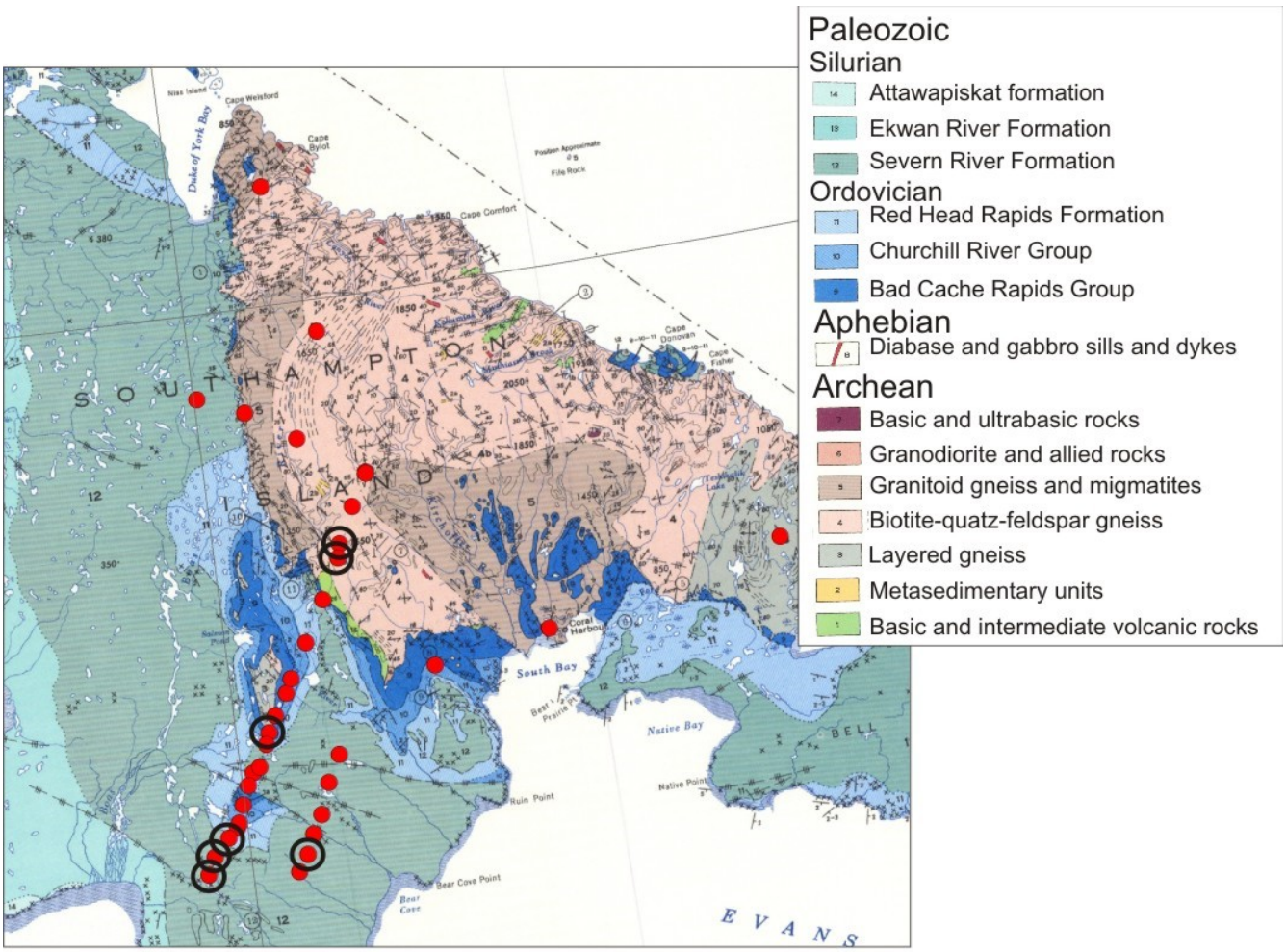
Paleozoic
Silurian
Attawapiskat formation
Ekwan River Formation
Severn River Formation
Ordovician
Red Head Rapids Formation
Churchill River Group
Bad Cache Rapids Group
Aphebian
Diabase and gabbro sills and dykes
Archean
Basic and ultrabasic rocks
Granodiorite and allied rocks
Granitoid gneiss and migmatites
Biotite-quatz-feldspar gneiss
Layered gneiss
Metasedimentary units
Basic and intermediate volcanic rocks
SOUTHAMPTON ISLAND
Cape Weisford
Cape Byiot
Cape Comfort
Cape Donovan
Cape Fisher
Coral Harbour
South Bay
Native Bay
Native Point
Ruin Point
Bear Cove Point
BELL
EVANS

Figure 4

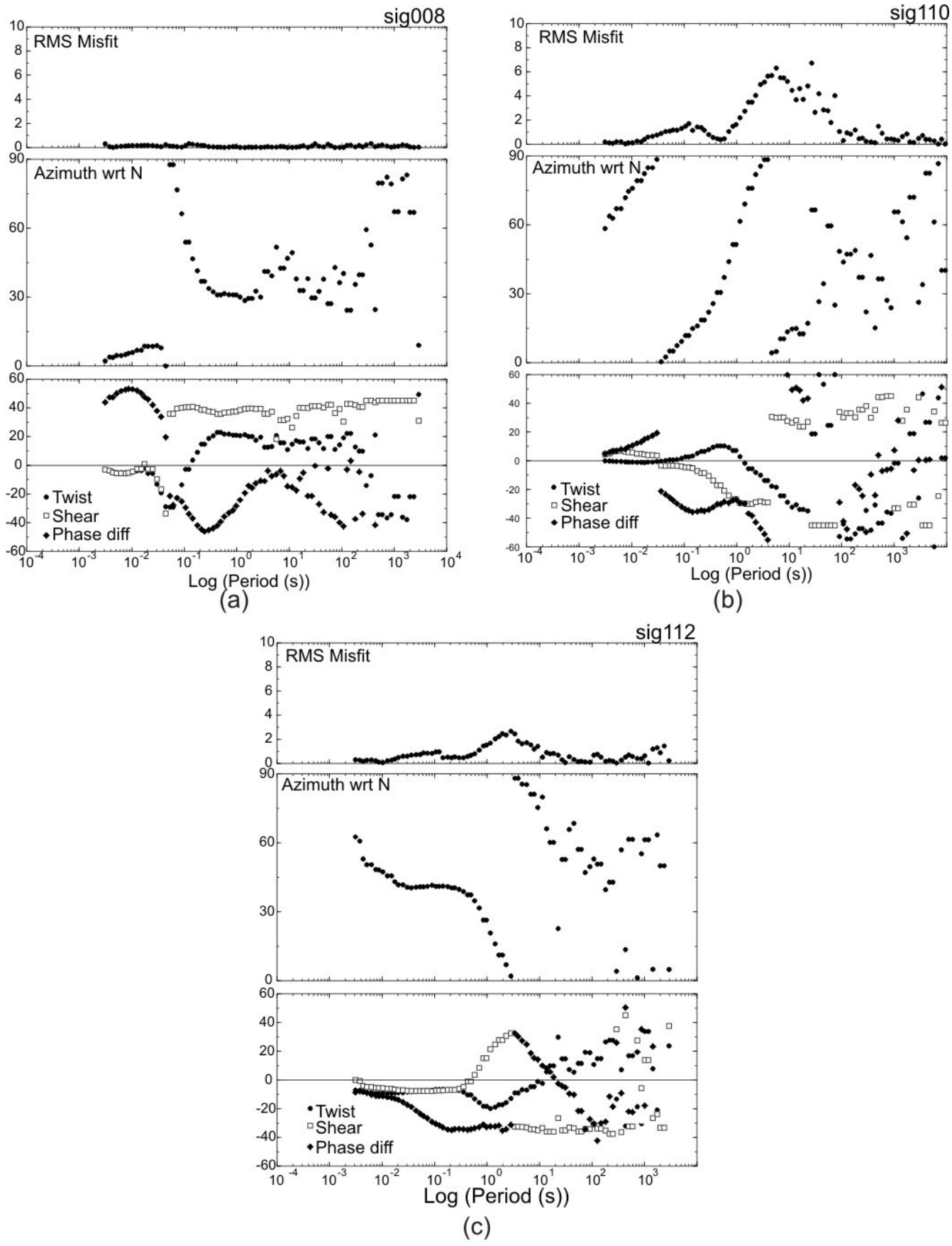
sig008
RMS Misfit
Azimuth wrt N
Twist
Shear
Phase diff
Log (Period (s))
(a)
sig110
RMS Misfit
Azimuth wrt N
Twist
Shear
Phase diff
Log (Period (s))
(b)
sig112
RMS Misfit
Azimuth wrt N
Twist
Shear
Phase diff
Log (Period (s))
(c)

Figure 5

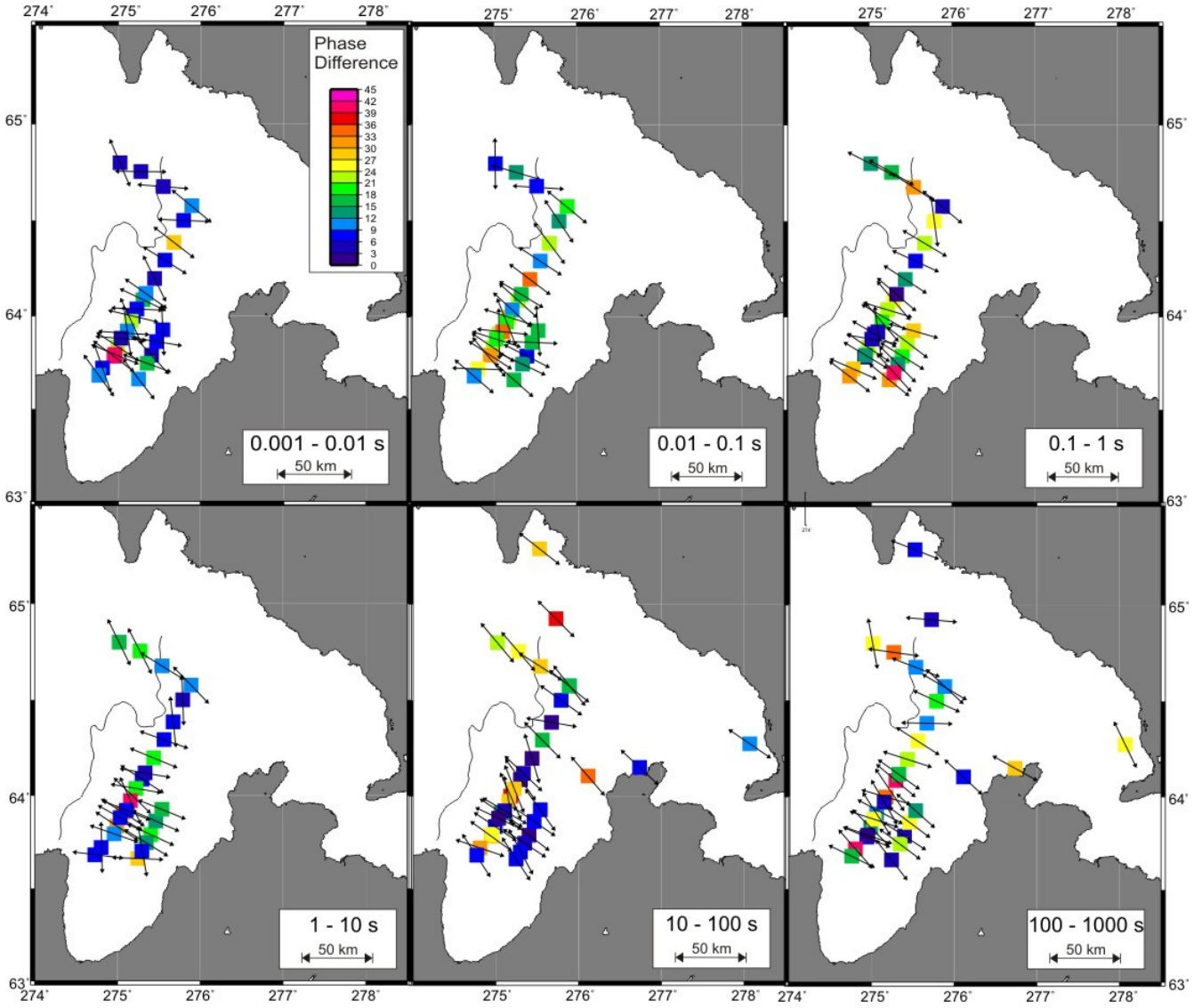
Phase Difference
45
42
39
36
33
30
27
24
21
18
15
12
9
6
3
0
0.001 - 0.01 s
0.01 - 0.1 s
0.1 - 1 s
1 - 10 s
10 - 100 s
100 - 1000 s
50 km
274°
275°
276°
277°
278°
63°
64°
65°

Figure 6

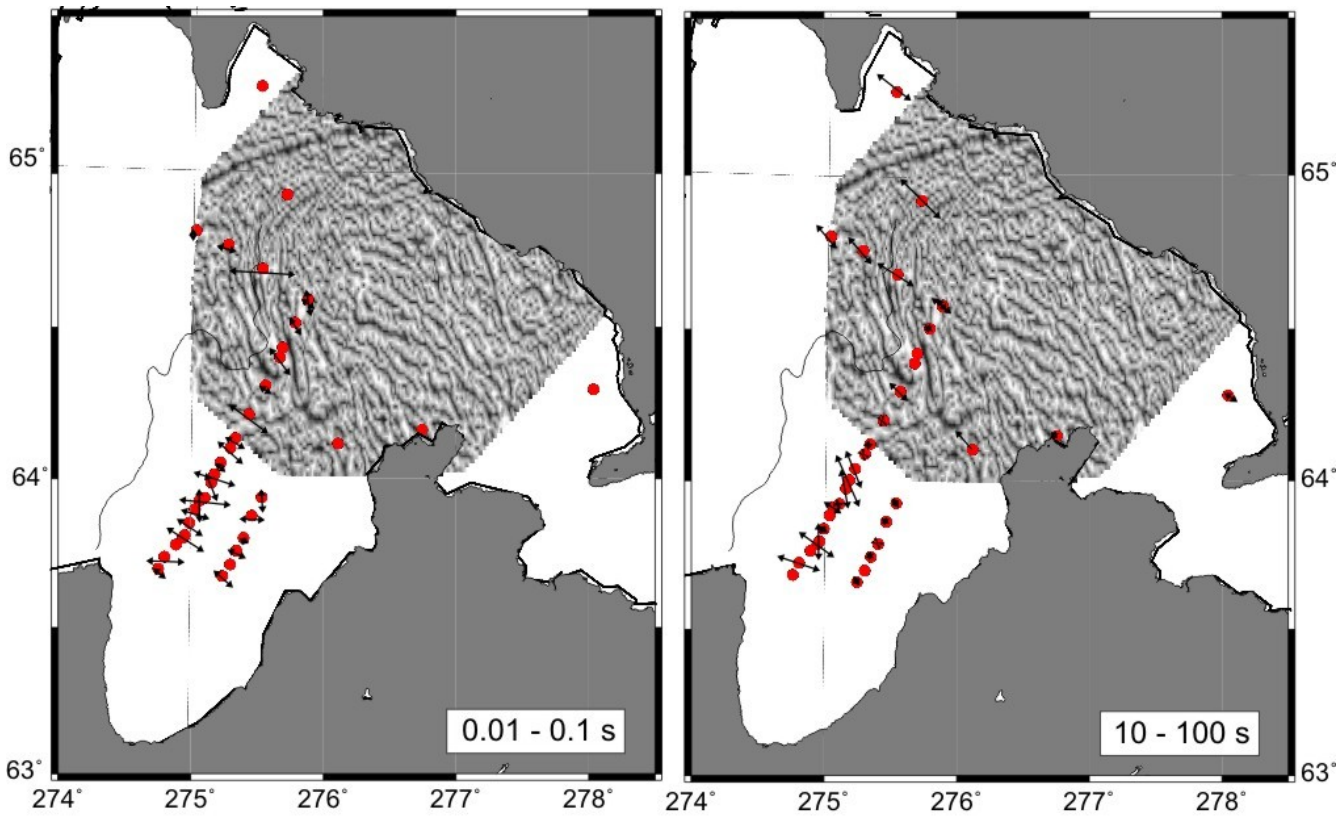


Figure 7

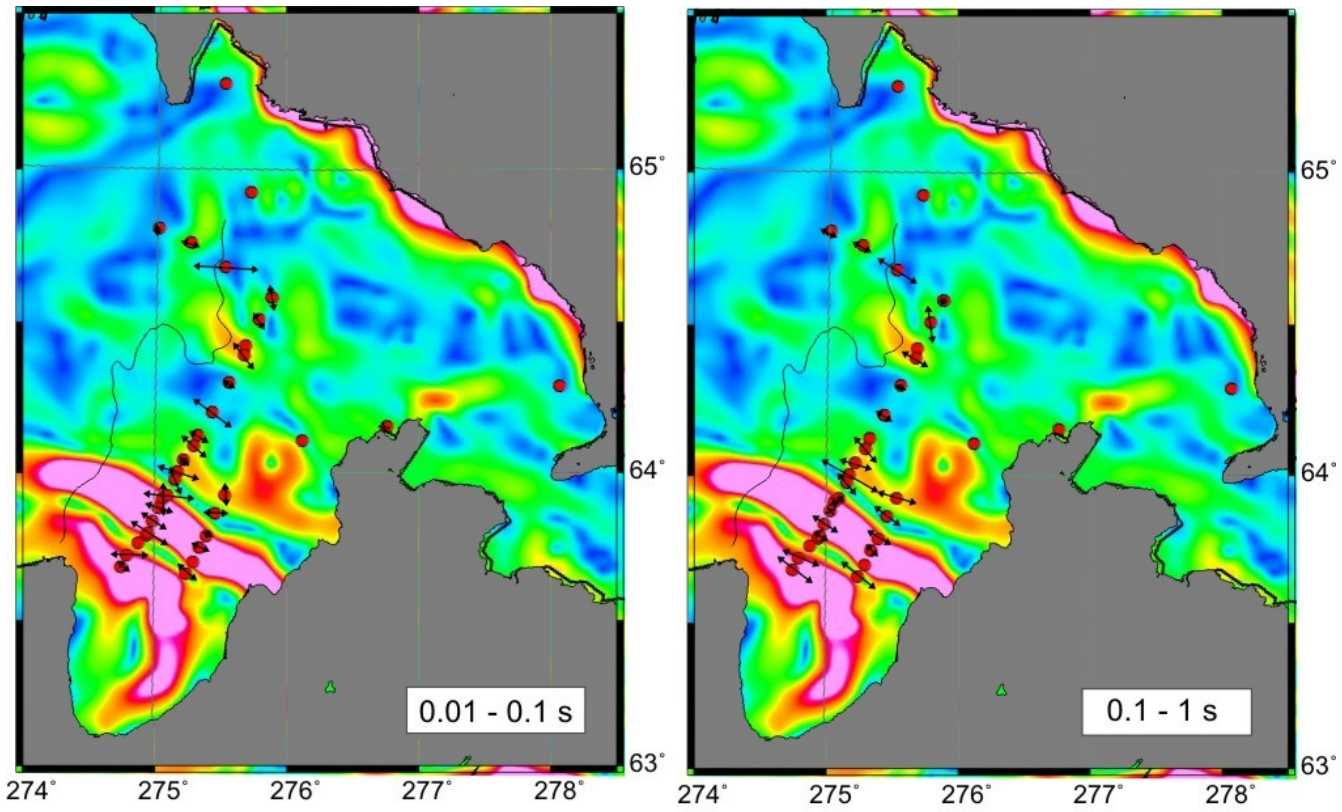


Figure 8

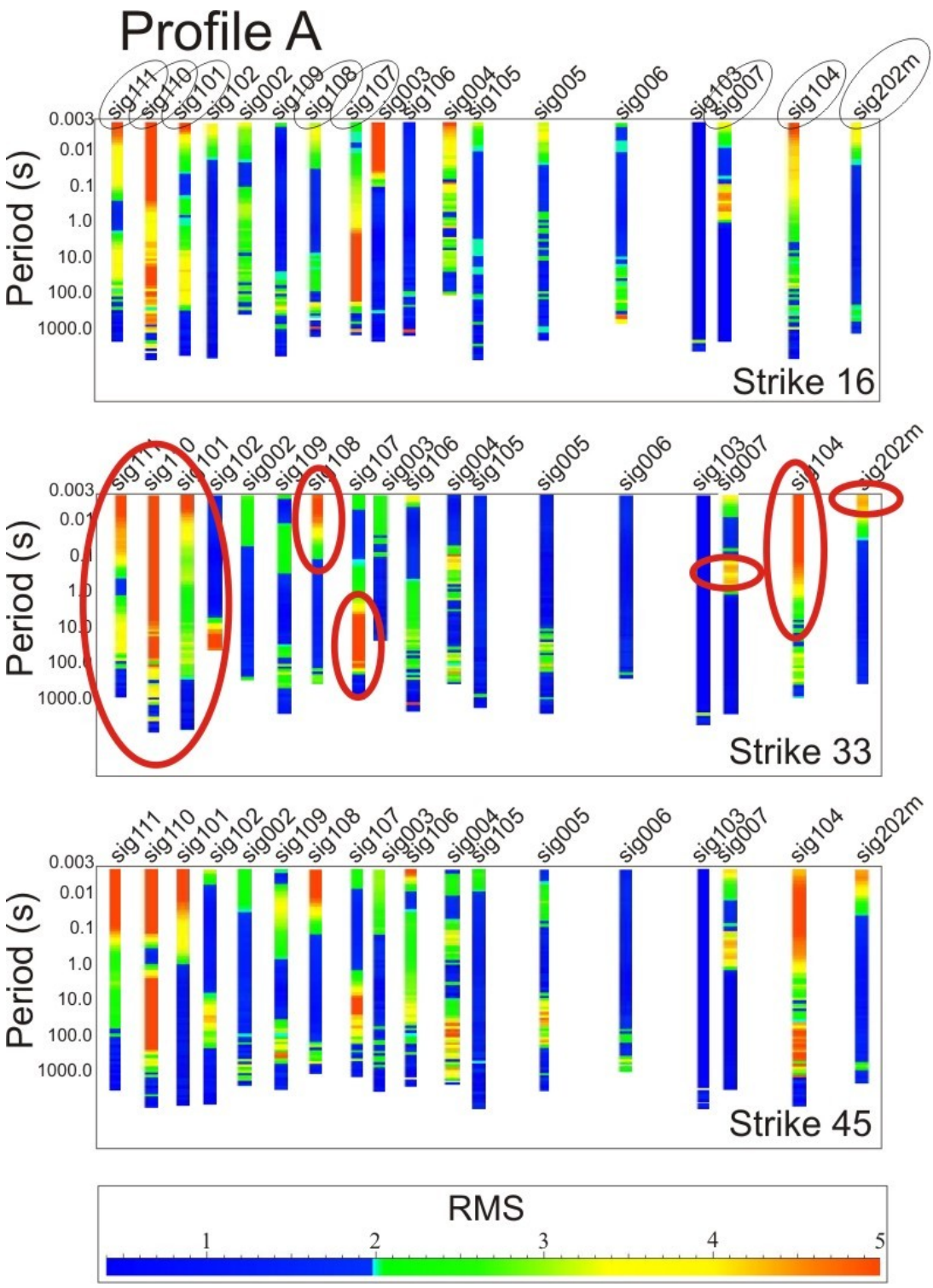
Profile A
sig111
sig110
sig101
sig102
sig002
sig109
sig108
sig107
sig003
sig106
sig004
sig105
sig005
sig006
sig103
sig007
sig104
sig202m
0.003
0.01
0.1
1.0
10.0
100.0
1000.0
Period (s)
Strike 16
Strike 33
Strike 45
RMS
1
2
3
4
5

Figure 9

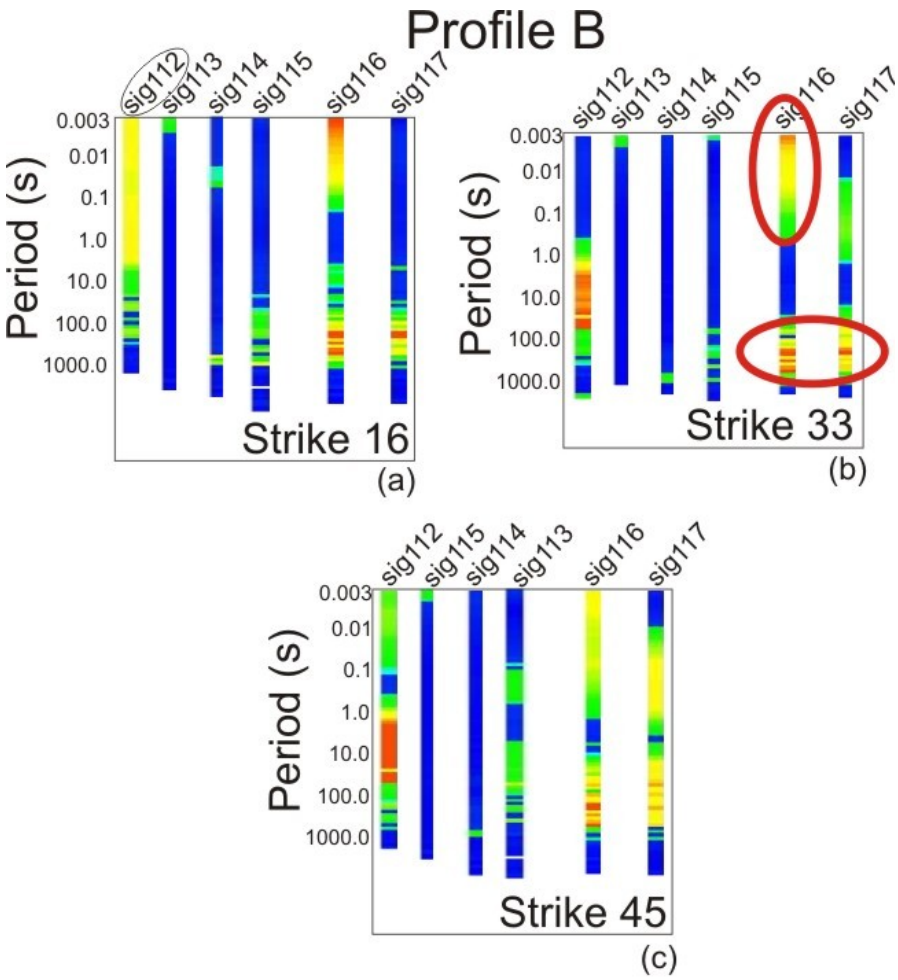
Profile B
sig112
sig113
sig114
sig115
sig116
sig117
0.003
0.01
0.1
1.0
10.0
100.0
1000.0
Period (s)
Strike 16
(a)
Strike 33
(b)
sig112
sig115
sig114
sig113
sig116
sig117
Strike 45
(c)

Figure 10

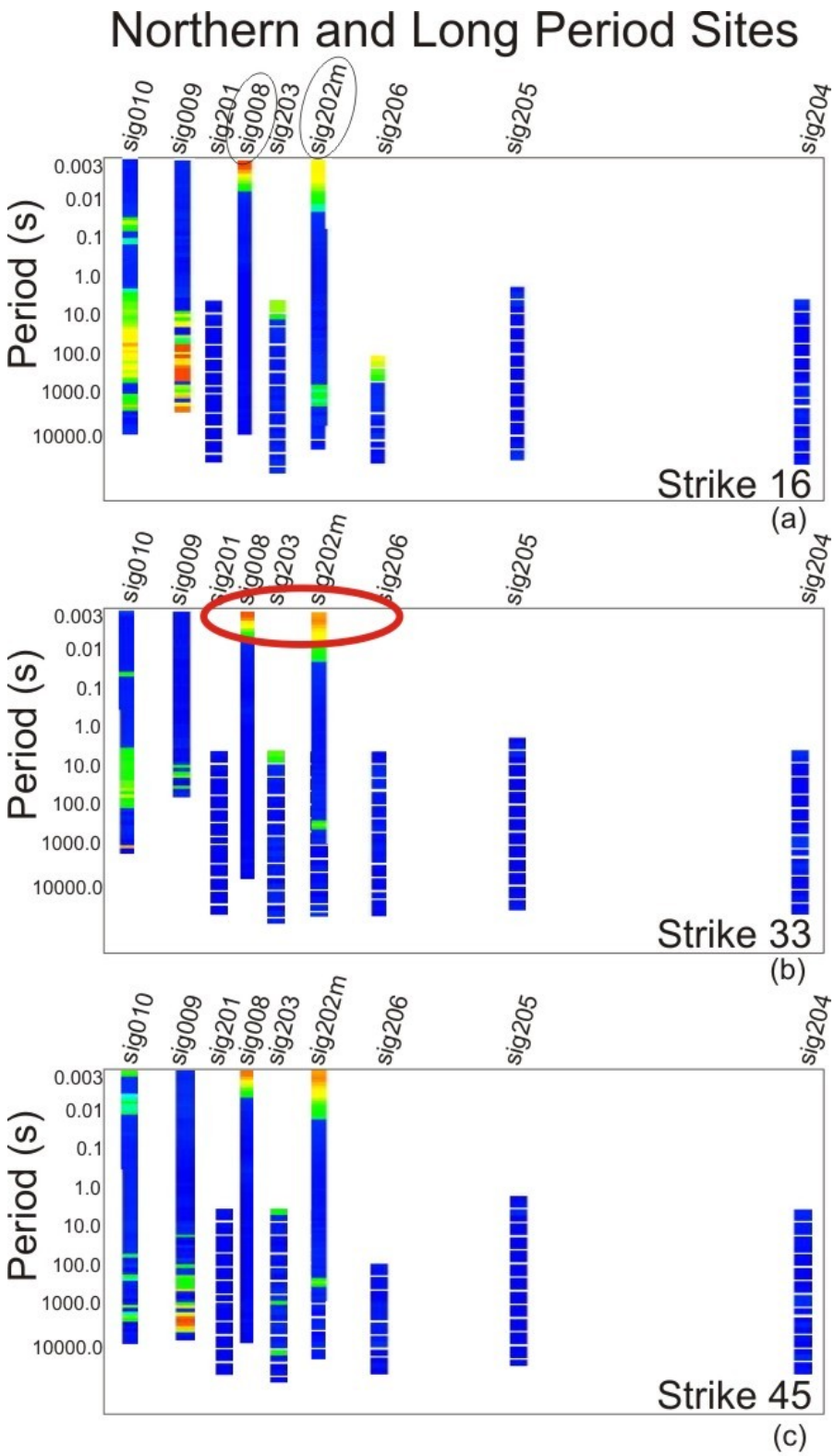
Northern and Long Period Sites
sig010
sig009
sig201
sig008
sig203
sig202m
sig206
sig205
sig204
Period (s)
0.003
0.01
0.1
1.0
10.0
100.0
1000.0
10000.0
Strike 16
(a)
Strike 33
(b)
Strike 45
(c)

Figure 11

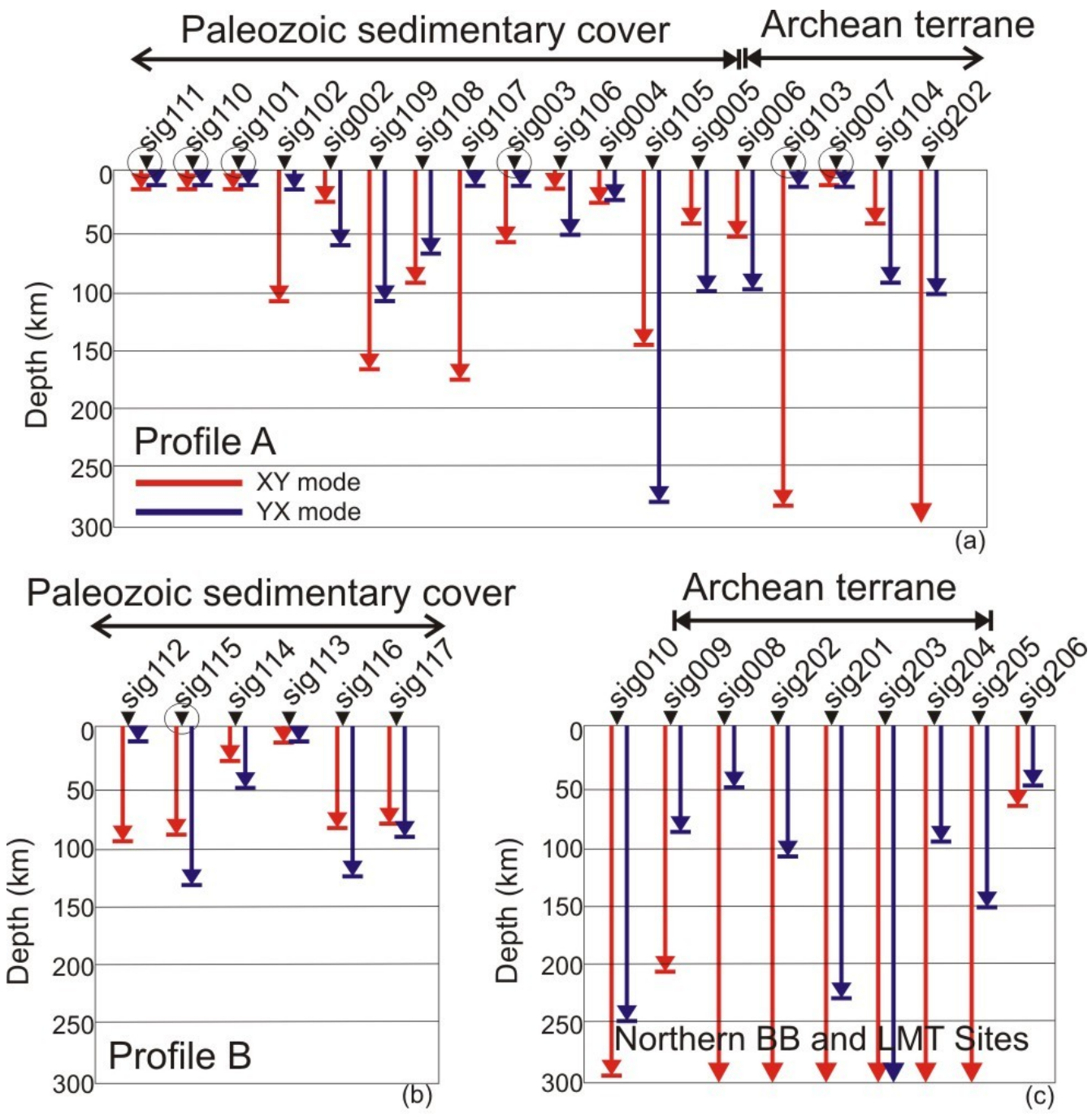
Paleozoic sedimentary cover
Archean terrane
sig111
sig110
sig101
sig102
sig002
sig109
sig108
sig107
sig003
sig106
sig004
sig105
sig005
sig006
sig103
sig007
sig104
sig202
Depth (km)
0
50
100
150
200
250
300
Profile A
XY mode
YX mode
(a)
Paleozoic sedimentary cover
sig112
sig115
sig114
sig113
sig116
sig117
Depth (km)
Profile B
(b)
Archean terrane
sig010
sig009
sig008
sig202
sig201
sig203
sig204
sig205
sig206
Depth (km)
Northern BB and LMT Sites
(c)

Figure 12

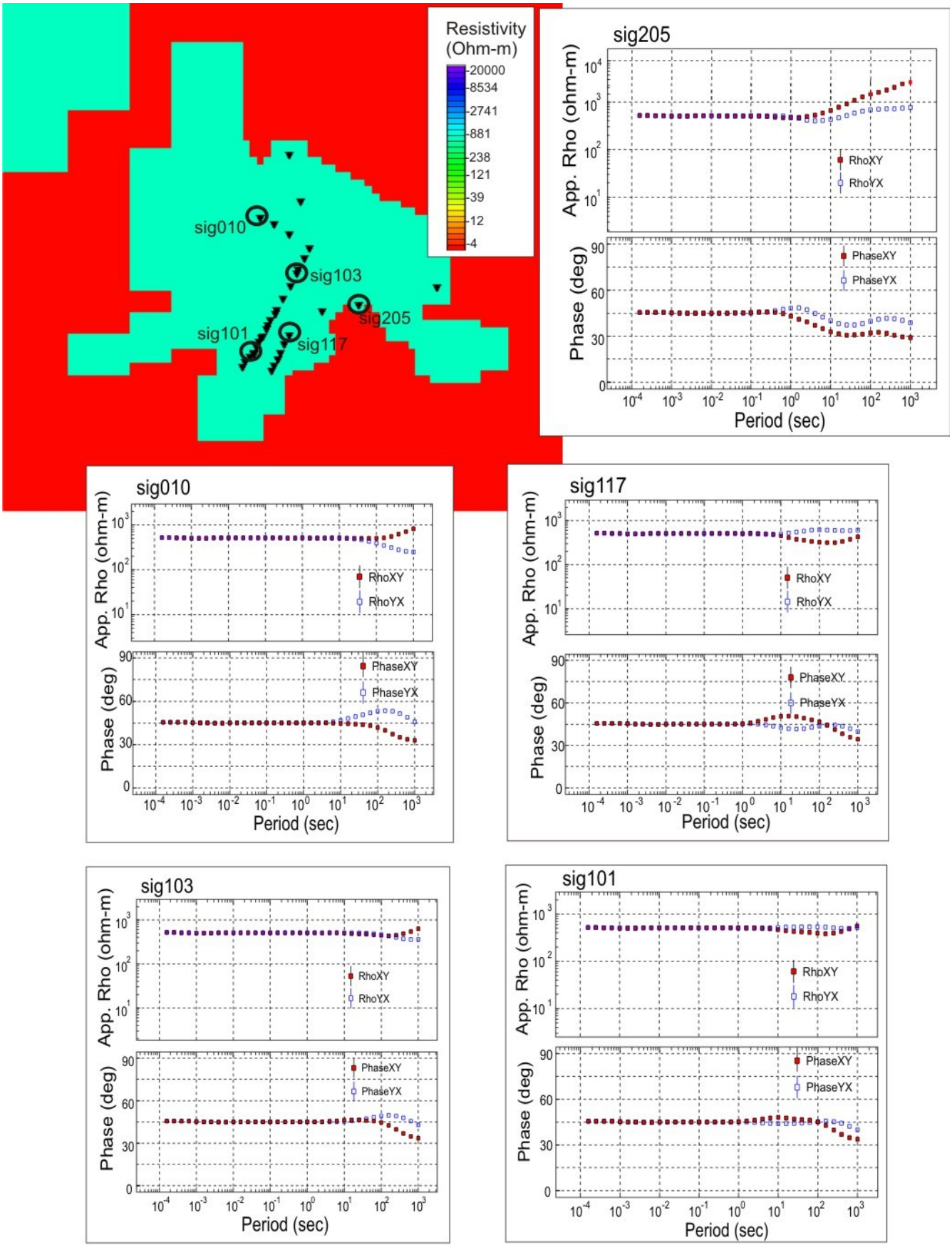
Resistivity
(Ohm-m)
20000
8534
2741
881
238
121
39
12
4
sig010
sig103
sig205
sig101
sig117
sig205
App. Rho (ohm-m)
RhoXY
RhoYX
Phase (deg)
PhaseXY
PhaseYX
Period (sec)
sig010
sig117
sig103
sig101

Figure 13

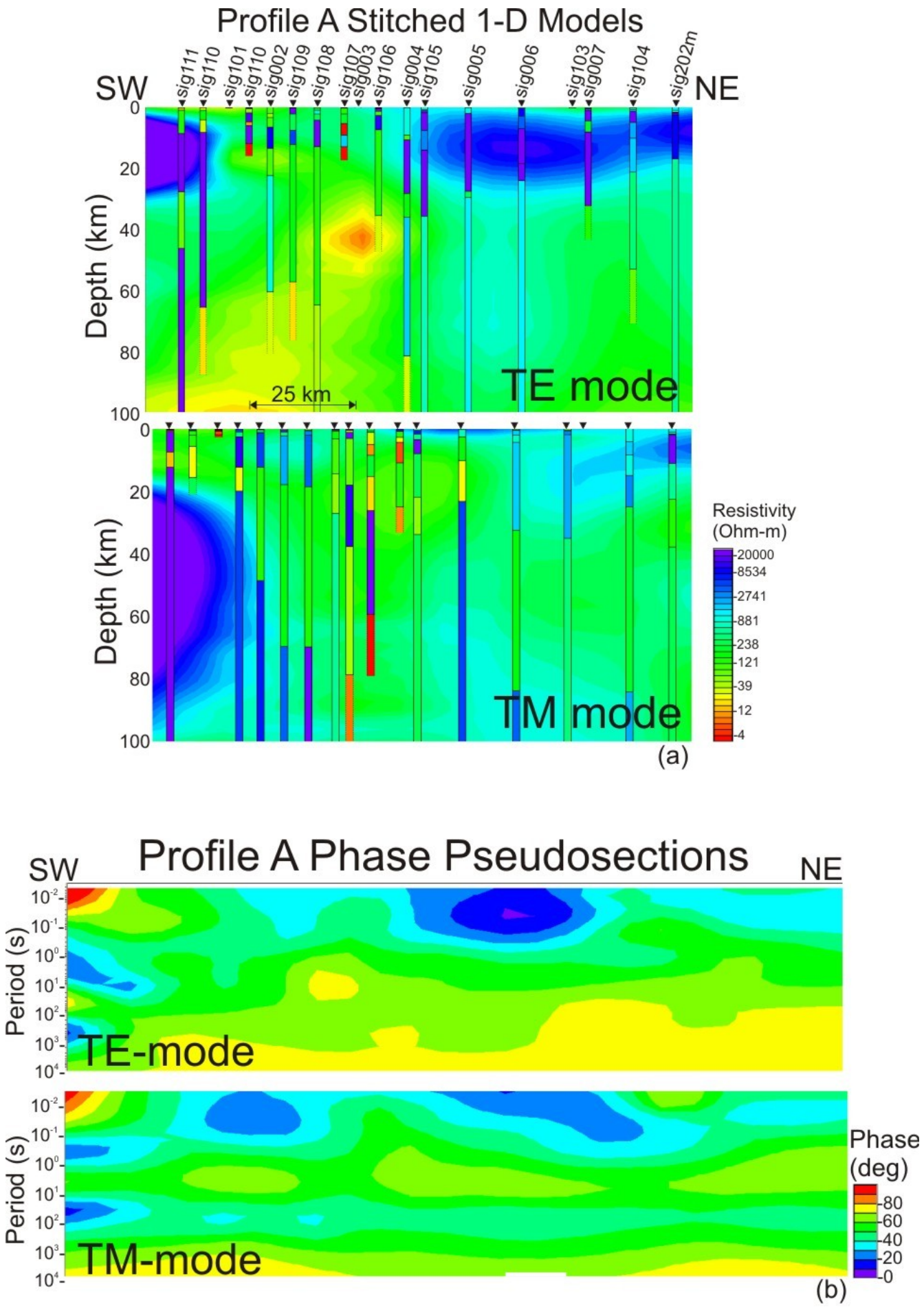
Profile A Stitched 1-D Models
SW
NE
sig111
sig110
sig101
sig110
sig002
sig109
sig108
sig107
sig003
sig106
sig004
sig105
sig005
sig006
sig103
sig007
sig104
sig202m
Depth (km)
0
20
40
60
80
100
25 km
TE mode
TM mode
Resistivity
(Ohm-m)
20000
8534
2741
881
238
121
39
12
4
(a)
Profile A Phase Pseudosections
SW
NE
Period (s)
TE-mode
TM-mode
Phase
(deg)
80
60
40
20
0
(b)

Figure 14

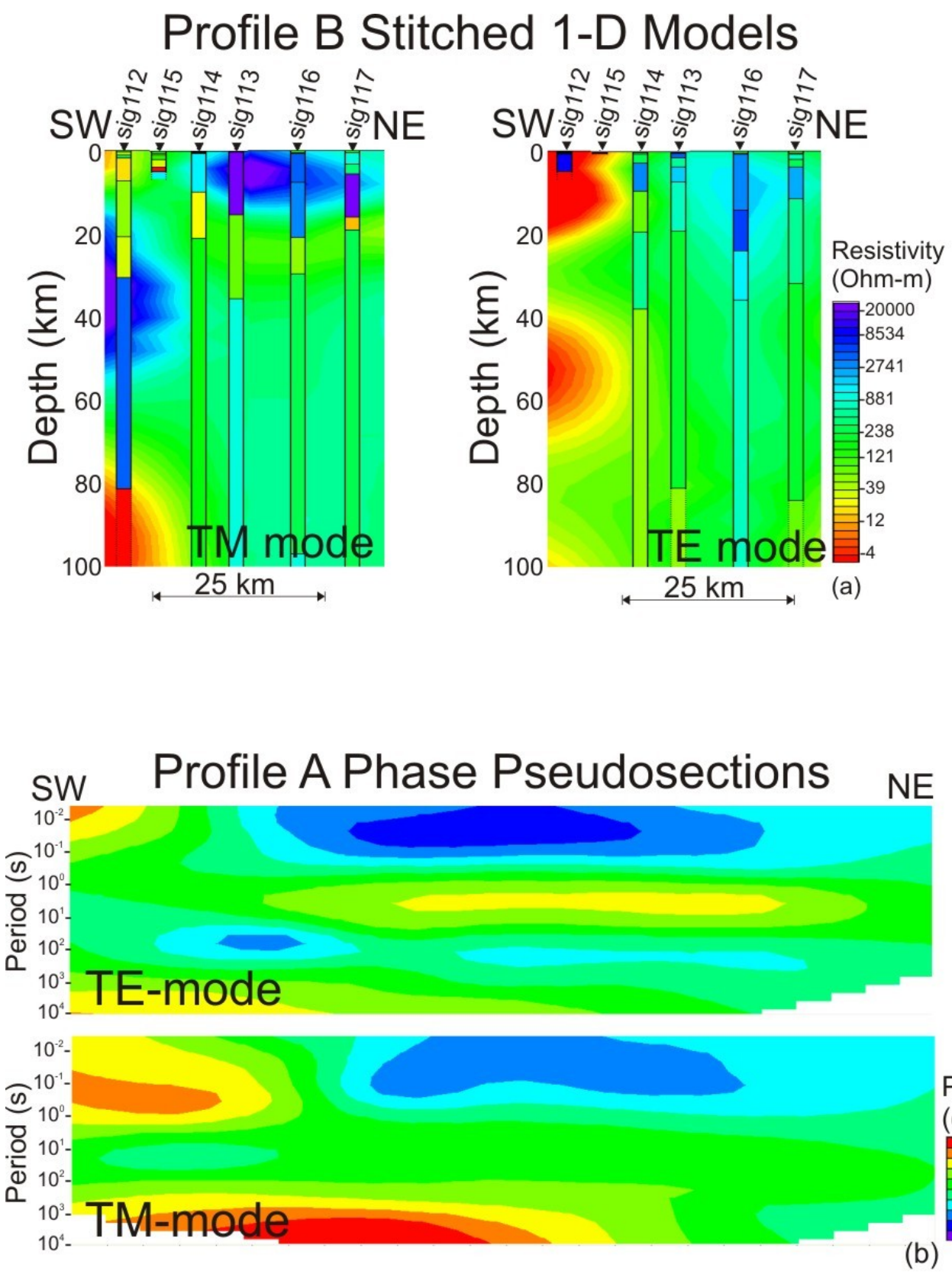
Profile B Stitched 1-D Models
SW
NE
sig112
sig115
sig114
sig113
sig116
sig117
Depth (km)
0
20
40
60
80
100
TM mode
TE mode
25 km
Resistivity
(Ohm-m)
20000
8534
2741
881
238
121
39
12
4
(a)
Profile A Phase Pseudosections
Period (s)
TE-mode
TM-mode
Phase
(deg)
80
60
40
20
0
(b)

Figure 15

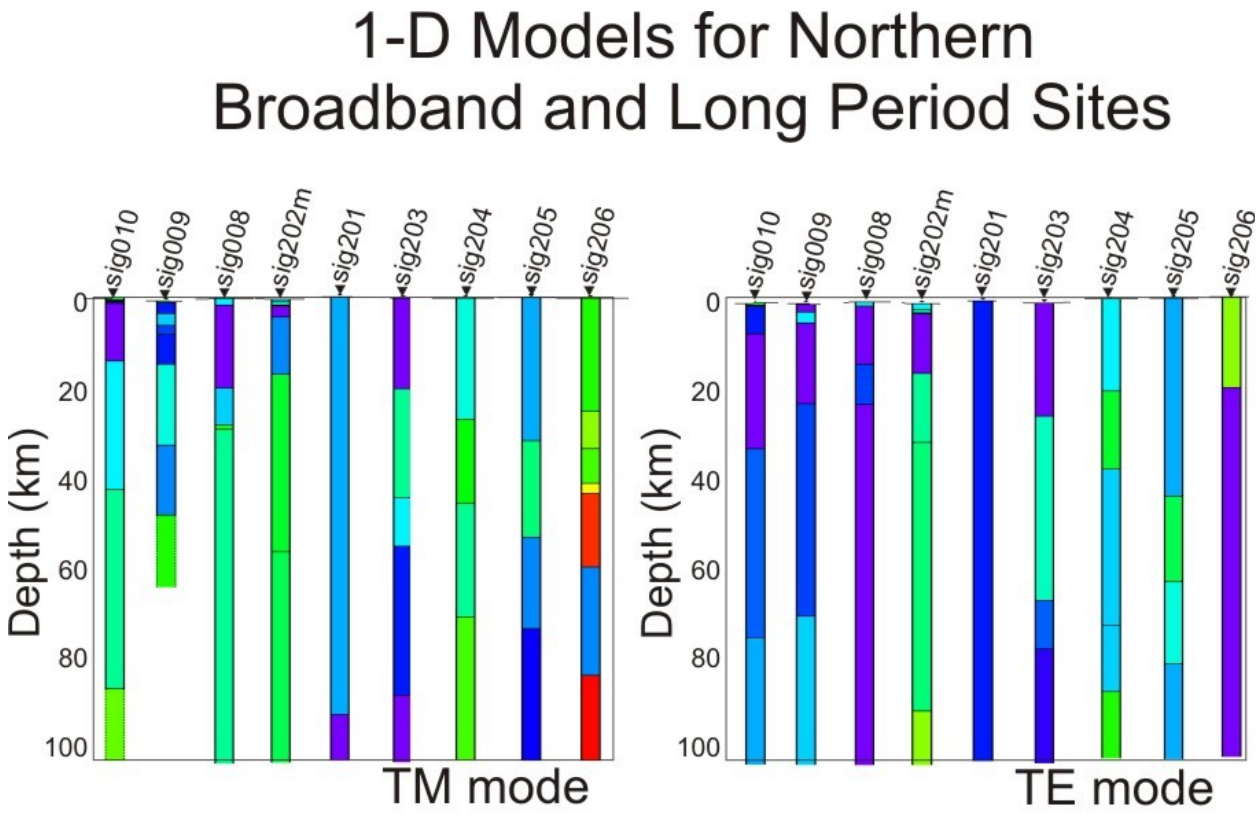


Figure 16

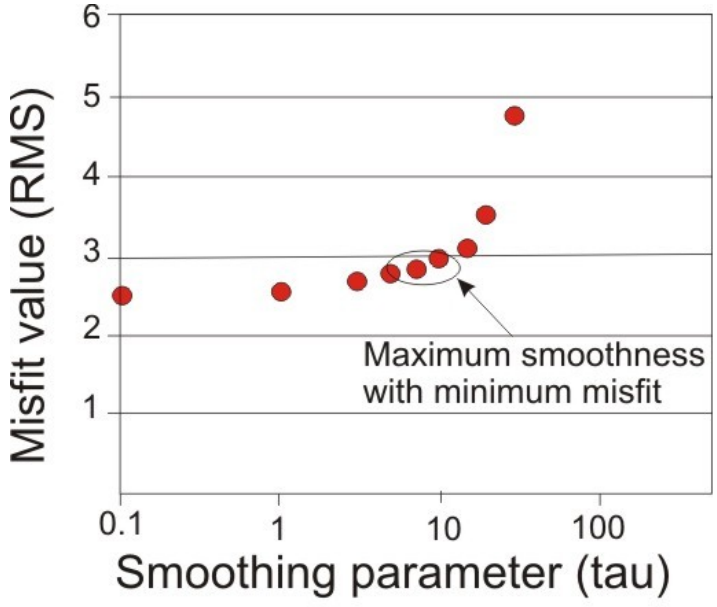


Figure 17

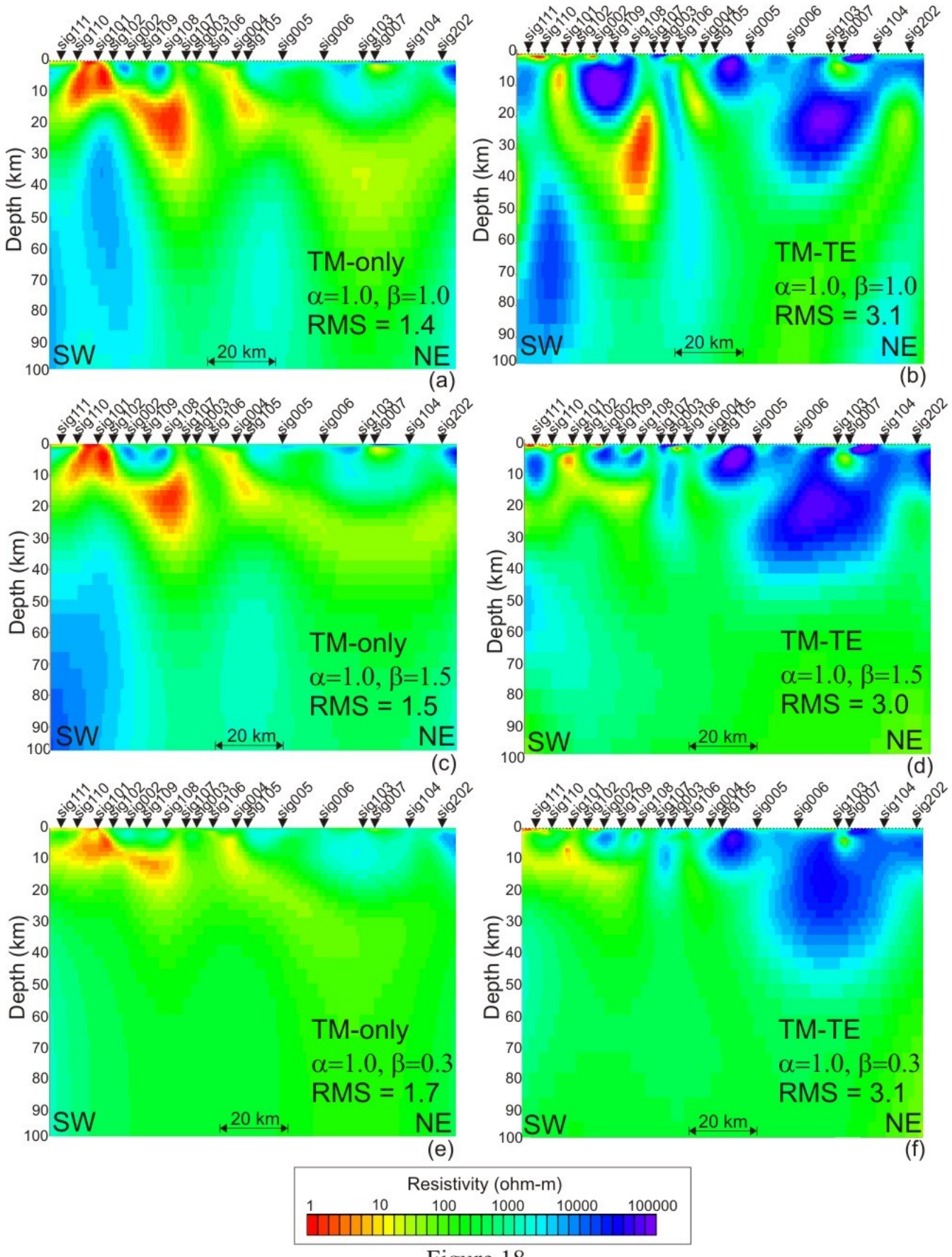
sig111 sig110 sig101 sig102 sig002 sig109 sig108 sig107 sig003 sig106 sig004 sig105 sig005 sig006 sig103 sig007 sig104 sig202
Depth (km)
0 10 20 30 40 50 60 70 80 90 100
TM-only
α=1.0, β=1.0
RMS = 1.4
SW
20 km
NE
(a)
TM-TE
α=1.0, β=1.0
RMS = 3.1
SW
20 km
NE
(b)
TM-only
α=1.0, β=1.5
RMS = 1.5
SW
20 km
NE
(c)
TM-TE
α=1.0, β=1.5
RMS = 3.0
SW
20 km
NE
(d)
TM-only
α=1.0, β=0.3
RMS = 1.7
SW
20 km
NE
(e)
TM-TE
α=1.0, β=0.3
RMS = 3.1
SW
20 km
NE
(f)
Resistivity (ohm-m)
1 10 100 1000 10000 100000

Figure 18

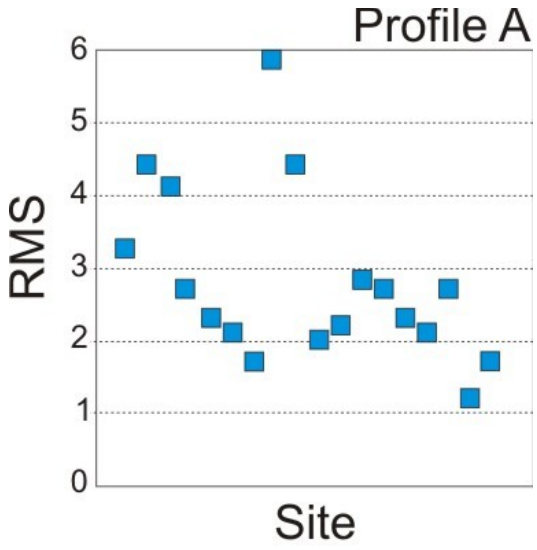


Figure 19

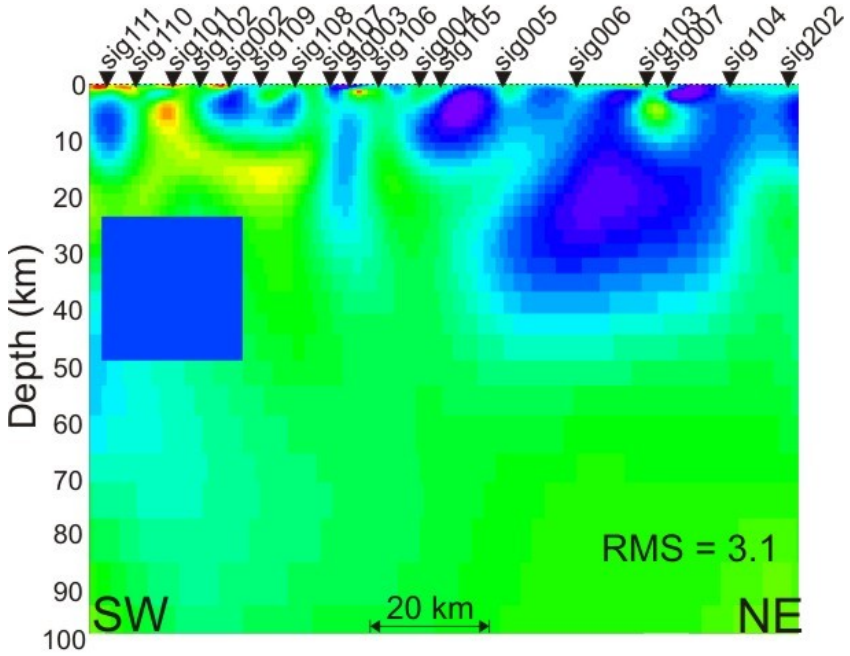


Figure 20

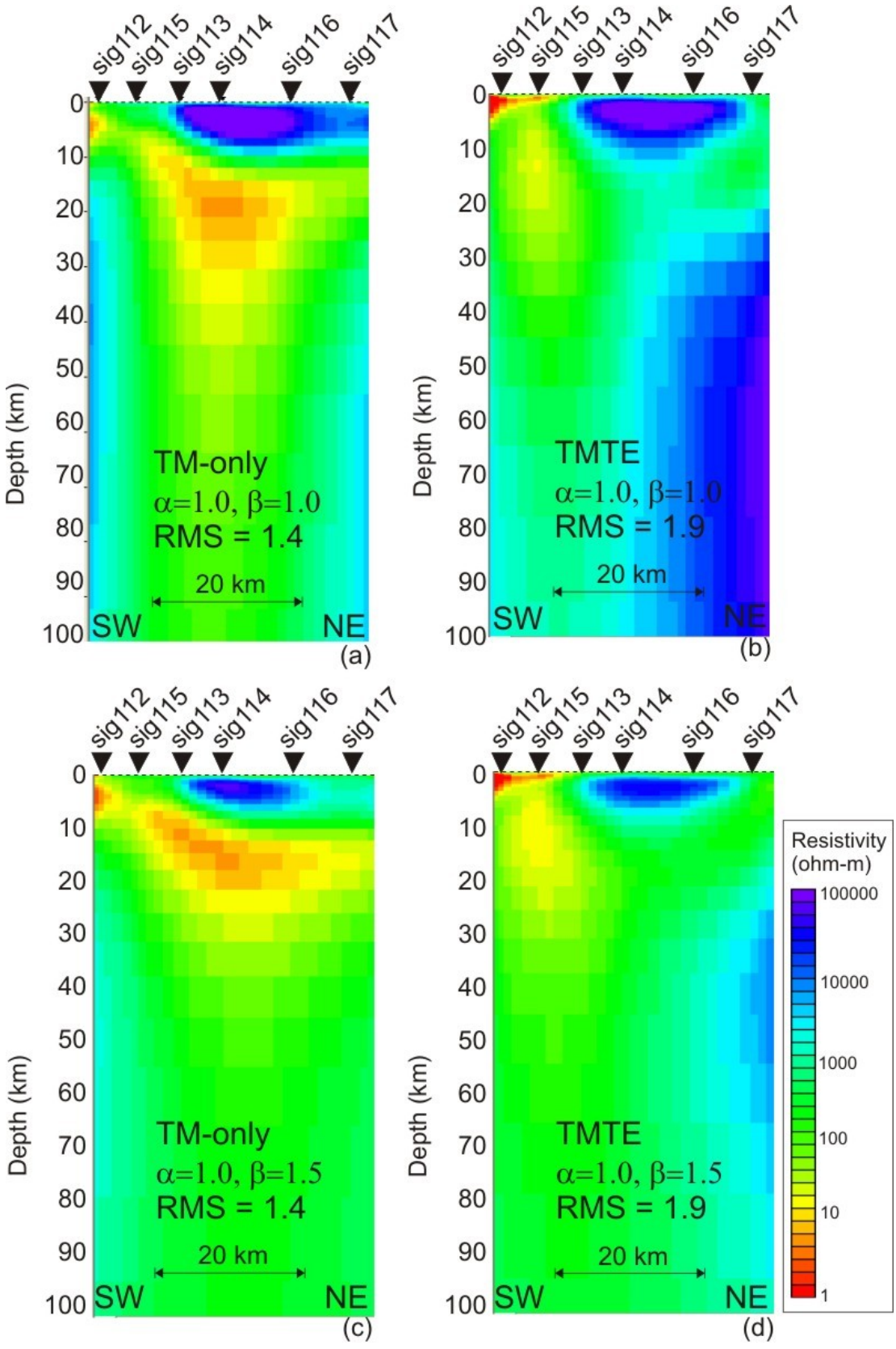
sig112
sig115
sig113
sig114
sig116
sig117
Depth (km)
TM-only
α=1.0, β=1.0
RMS = 1.4
20 km
SW
NE
(a)
TMTE
α=1.0, β=1.0
RMS = 1.9
(b)
TM-only
α=1.0, β=1.5
RMS = 1.4
(c)
TMTE
α=1.0, β=1.5
RMS = 1.9
(d)
Resistivity
(ohm-m)
100000
10000
1000
100
10
1

Figure 21

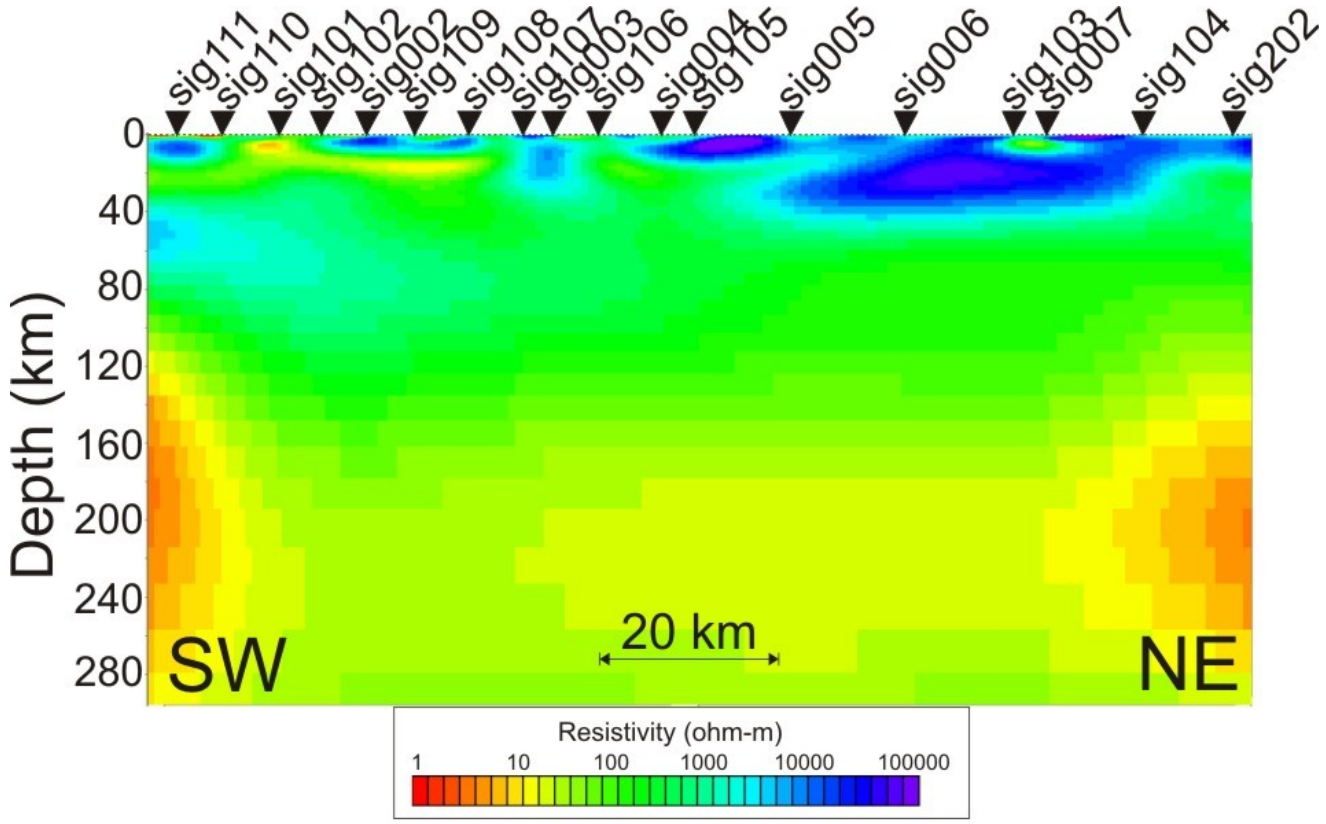
sig111
sig110
sig101
sig102
sig002
sig109
sig108
sig107
sig003
sig106
sig004
sig105
sig005
sig006
sig103
sig007
sig104
sig202
0
40
80
120
160
200
240
280
Depth (km)
SW
20 km
NE
Resistivity (ohm-m)
1
10
100
1000
10000
100000

Figure 22